LBL-18840
UC-21 c.2

Lawrence Berkeley Laboratory
UNIVERSITY OF CALIFORNIA

Accelerator & Fusion Research Division

HEAVY ION FUSION END OF THE YEAR REPORT
April 1, 1984 -- September 30, 1984

Heavy Ion Fusion Staff

December 1984

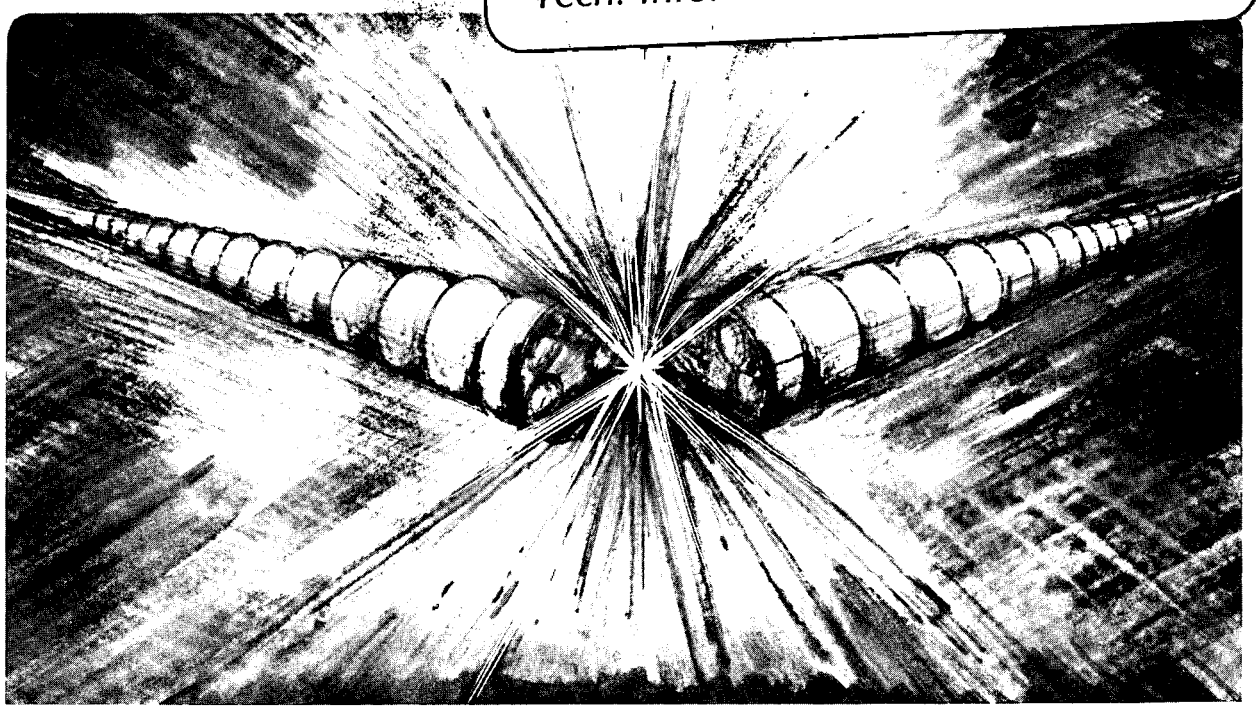

Prepared for the U.S. Department of Energy under Contract DE-AC03-76SF00098

DISCLAIMER

LBL-18840
HIFAN-265

Heavy Ion Fusion End of the Year Report*

April 1, 1984 – September 30, 1984

Heavy Ion Fusion Staff

Accelerator and Fusion Research

Lawrence Berkeley Laboratory
University of California
Berkeley, California

December 1984

*This work was supported by the Office of Energy Research, Office of Basic Energy Sciences, U.S. Department of Energy under Contract No. DE-AC03-76SF00098.

Contents

Page

Highlights 1

Multiple Beam Experiment (MBE):
Conceptual Design and Program Description 3
1. Introduction 3
2. The MBE-16 Design 4
3. Four-Beam Multiple Beam Experiment (MBE-4) 5

Theory 11
1. Current Amplification in MBE-4 11
2. Transverse Simulation Results 12
3. Longitudinal Phenomena in MBE and HTE 13
4. High Temperature Experiment System Model 14

Single Beam Transport Experiment 17
1. Transverse Focusing Experiments 17
2. Longitudinal Beam Experiments 18

Neutralized Beam Focusing Experiment 21

Range Energy Measurements 23

Source Development Work 27
1. K^+, Na^+, Cs^+ Emission from Alumino Silicates 27
2. A Candidate Design for MBE-4 Cs^+ Injector 27
   2.1 Ion Source 27
   2.2 Gun Optics 29
   2.3 Gun Layout 30
   2.4 Matching Section 35
   2.5 Fallback Position 35

Induction Linac Component Development 37
1. 200 kV Test Stand 37
   1.1 Astron Column Breakdown Voltage Measurements 37
   1.2 Conditioning Behavior of Insulators 39
2. Insulator Development 39
   2.1 Outgassing Measurements 39
   2.2 Large Polysil Insulator 43
   2.3 Bonded Insulator Development 43
   2.4 Cast Epoxy Insulator Development 47

3. Metglas Core Tests 48
3.1 Experimental Results 48
3.2 Conclusions 53

Publications 55

H.I.F. Staff Roster 57

Distribution List 59

List of Figures

Figure	Caption	Page
1	Site plan showing multiple beam induction linac located in existing Building 58 complex	7
2	MBE-4 longitudinal cross-section	8
3	Scale comparison MBE-16 and MBE-4	9
4	Energy and mass number boundaries for an Al target heated to 80 eV. The high A are excluded by shortness of range, low A are excluded by target disassembly, and low E are excluded by the perveance condition	15
5(a)	Gun voltage, left, and bunch current, right, with and without positive ear at tail of pulse	19
5(b)	Gun voltage, left, and bunch current, right, with and without negative ear at front of pulse	19
6(a)	Positive voltage perturbation, off and on, on high intensity beam. 2μs/div.	20
6(b)	Positive voltage perturbation on low intensity beam	20
7	Space charge potential outside beam as a function of position. T_F = 2400°K, B = 0	22
8	Range-energy relation for Au ions in CH and Au. Data are preliminary. Curves are based on scaling of the proton range-energy relation and the range-extension of heavy ions due to charge neutralization	25
9	Measured energy-loss rates of Au ions in CH and Au. Data are preliminary. Curves are described in Fig. 8	26
10	Emission current density limits for alumino-silicate sources of alkali ions	28
11(a)	Emission from a Cs^+ alumino-silicate. The straight line is the Child Langmuir prediction ($V^{3/2}$) for a planar diode with a somewhat uncertain normalization	31
11(b)	Emission uniformity from a Cs^+ alumino-silicate source	31

12	Emittance angles versus emission current density from a Cs^+ alumino-silicate	32
13	Optics design of MBE-4 diode	33
14	Beam profiles and divergence angles from the MBE-4 diode design	34
15	A matching solution for 10mA of Cs^+ at 200V in MBE-4	36
16	Breakdown tests of Astron column	38
17	Conditioning of a quartz insulator	40
18	Conditioning of an alumina insulator	41
19	De-conditioning of an alumina insulator	42
20	Vacuum outgassing of bisphenol A epoxy	44
21	Vacuum outgassing of bisphenol A epoxy filled with 40 μm glass beads	45
22	Vacuum outgassing of epoxy novolac filled with 40 μm glass beads	46
23	DC hysteresis loop for Metglas 2605S-2 (f = 0.1 Hz)	49
24	Typical voltage-current data for Metglas 2605S-2	50
25	Pulsed loss data adjusted for stacking factor, f = 1	51
26	Induction module design exercise showing improved performance for Metglas 2605SC and 2605S-2	54

Highlights

The past six months have seen important advances in the design of the upcoming Multiple-Beam Experiment (MBE), new results from the ongoing Single Beam Transport Experiment (SBTE), strong theoretical activity both in support of these experiments and also addressed to broader issues, and a strengthened R and D program related to future accelerator design. We note, in particular:

(1) The first convincing engineering design for a 16-beam induction-linac experiment, MBE-16, emerged in May 1984 in which a self-consistent — but probably not optimum — integration of components and their functions was evident. This preliminary design received a favorable review by the DOE and consultants after a two-day meeting in June at LBL.

(2) The news in mid-July, that the 80% budget increase hoped for in FY 85 would not be sanctioned by Congress caused an abrupt change in planning. The intended review and optimization of the MBE-16 design was abandoned. Instead, a scaled-down multiple beam experiment with four beams, called MBE-4, became the subject of examination. The objective was to build a proof-of-principle experiment to demonstrate beam-power amplification with multiple beams, and modeling as many features of the future High Temperature Experiment (HTE) as possible. In order to meet budget constraints, MBE-4 has been designed to re-use existing components and materials, insofar as possible.

(3) A revised HIFAR program plan was presented to DOE in September describing the proposed MBE-4 design, and arguing for the continuation of work on the 16-beam injector tests at LANL but on a somewhat stretched time scale.

(4) Some remarkable new theoretical results on transverse beam dynamics for space-charge-dominated beams have emerged from simulation, computation and analysis. These activities are best described as "work-in-progress":

   (i) Imperfect electrostatic quadrupole design can result in a dodecapole component of the field. Emittance growth is not seen for on-axis beams but can be significant for off-axis beams.

   (ii) Provided the beam radius does not exceed 80-85% of the aperture, the image forces have little effect on emittance for on-axis beams. If mis-steered, however, a beam exhibits a strong oscillation in r.m.s. emittance —

modulated by a low-frequency beating — according to the simulation results. Analytic work accounts for the oscillatory-beat behavior in terms of a resonance between the coherent betatron oscillation and a third-order mode, but cannot yet shed light on the accompanying monotonic growth in emittance seen in the simulation work.

(iii) A surprising amelioration of the bad effects due to images for off-axis beams is observed by simulation if external field nonlinearities (dodecapole) are introduced.

(5) A preliminary map of the allowable boundaries in multidimensional parameter space for the HTE has been developed.

(6) The SBTE has established that (within experimental errors of a few percent) emittance is preserved and no particle loss occurs for a single-particle betatron phase-advance, $\sigma_0 = 60°$, and depressed phase advance, $\sigma = 8°$. The experiment has failed to detect any limiting minimum value of σ, for $\sigma_0 < 90°$. For σ_0 above 90°, limiting minimum values of σ — below which beam loss and emittance growth occur — have been mapped systematically as a function of σ_0.

(7) The effect of a discrete energy jump partway along a beam bunch is being studied theoretically with a 1-D PIC code, and experimentally with the SBTE. At low-currents, bunching occurs while, at high current, plasma waves produce a smoothing effect.

(8) Development of high brightness sources continues and a nested array of four sources for MBE-4 has been designed.

(9) The 2 1/2-D PIC code MASK is helping in the understanding of the discrepancies between the experimental performance of the Robertson lens experiment and the simplified theory — effects that appear to be explained by non-zero electron temperature.

(10) The first (of three) experimental runs at the Bevalac to measure the range energy relation for gold ions in light and heavy cold condensed targets have shown remarkable agreement with theoretical scaling laws, at least for the high charge-state ions used so far (Z = 61).

(11) The program on exploring insulator performance for different arrangements of grading rings and different materials, has been intensified. Other considerations that enter into the identification of desirable insulators are also being evaluated; these include cost, scalability to large size, outgassing rate, and mechanical properties. A systematic test program for a variety of cast plastic formulations has begun.

(12) An extensive set of measurements on small test cores of Metglas has been carried out for different materials and a variety of annealing histories, preparatory to purchasing significant quantities of this material from Allied Chemical.

Multiple Beam Experiment (MBE): Conceptual Design and Program Description

1. Introduction (HIFAR Group)

Much of our effort during this reporting period has been spent in the design of a Multiple Beam Experiment (MBE-16) that was to be constructed and installed at the Lawrence Berkeley Laboratory. This experiment was intended to: a) demonstrate much of the accelerator physics; and b) develop technology on the scale necessary for the High Temperature Experiment (HTE). The MBE-16 was identified in the 1983 research plan[1] as a direct route to the High Temperature Experiment (HTE). However, Congressional budget actions in July 1984 have made it clear that this experiment cannot be carried out in the near future. As a consequence, the MBE-16 has been redefined as a smaller experiment, the MBE-4, that will model much of the HTE accelerator physics but can do little to develop the HTE technology.

A redefined and scaled down program has been developed that is consistent with the FY 85 budget and beyond.[2] This new program is designed to accomplish the following:

1) Proceed as rapidly as possible with a scaled-down Multiple Beam Experiment (called MBE-4, reflecting the choice of 4 beams) to constitute a proof-of-principle accelerator which can produce some results in FY 85 and significant results in FY 86. MBE-4 is described further in Section 3 which follows the MBE-16 description.
2) Maintain the 2 MeV, 16-beam, high-current injector program at LANL in its present form as a technology development demonstration for HTE, but with a slip in schedule to late FY 86. Postpone fabrication of the matching/diagnostics section until FY 86.
3) Postpone the development, fabrication and testing of large 16-beam HTE-size accelerating units until FY 86 and FY 87. In FY 85, small-scale component development will continue but at a modest pace.

1. *Heavy Ion Fusion Accelerator Research Program Plan for FY 84-FY 89.* Compiled by R.O. Bangerter, Los Alamos National Laboratory Report LA-UR-1717 (1983).

2. *Revised MBE Program Plan*, Sept. 1984, LBL Report PUB-5123.

4) Continue experiments with the Single Beam Transport Experiment (SBTE) until the end of FY 85.

The foregoing plan is directed towards a position in FY 87 in which most of the novel physics of HTE will have been demonstrated at reduced scale on MBE-4 and in which many of the large-scale components for HTE (16-beam injector, matching, some acceleration) will have been shown so that one can proceed with confidence to build HTE.

2. The MBE-16 Design

An initial design for MBE-16 is described in a report[3] that documents the present state-of-the-art of ion induction accelerator technology on the HTE scale and points to areas where future development can significantly reduce the cost of the HTE. The 16 beamlets (up to 6 μs in duration) would have been obtained from a source/injector being developed at the Los Alamos National Laboratory. Each beamlet is generated on a spherical hot surface and electrostatically accelerated to 2 MeV through a series of electrodes inside an evacuated alumina insulating column. The column is powered by a "sag-compensated" Marx generator with a triggered diverter switch that ends the current pulse.

At the output of the injector each beamlet passes through a matching section consisting of ten quadrupole arrays. Interspersed between the quad arrays are steering and diagnostic sections that will allow the beams to be steered into the accelerator. With the adjustment of the quad voltages, the LANL beams can be precisely matched into the MBE-16 accelerator.

Through the entire MBE-16 accelerator and transport sections the 16 beamlets are contained and focussed by an electrostatic quadrupole array consisting of 32 electrodes arranged in a rectangular grid so as to form apertures for 21 beamlets. To facilitate beam handling, only the outer 16 apertures will be occupied. The quad arrays are arranged in a FODO lattice with a period of 63 cm.

The MBE-16 linac will consist of 25 combined focusing and induction units which are a full lattice period (63 cm) long, each unit containing two electrostatic quad arrays for focussing the 16 parallel beams. Fourteen induction cores are contained in each unit and can generate up to 175 kV for 3 μs across a single accelerating gap. The cores are powered by individual pulsers whose firing times are varied to generate the proper voltage waveform for obtaining current amplification.

Acceleration schedules, consisting of particular combinations of induction unit voltage waveforms, are presented. They show that, typically, the MBE-16 accelerator will be capable of accelerating 2 MeV cesium ion beams 1.3 μs long to nearly 4 MeV at beam head and 6 MeV at beam tail with a current amplification of approximately 1.6 from 2.4 A to 3.5 A. Many other acceleration schedules are possible and will be investigated in the course of the research.

The conceptual design has revealed that all parts of the MBE-16 accelerator can be fabricated with current technology. Assuming that the MBE-16 were to be constructed as a research project (i.e. including LBL overhead), the total cost of the facility, based on today's technology and on only a preliminary design, is estimated to be approximately 28 M$. The

3. *Multiple Beam Experiment (MBE-16): Conceptual Design and Program Description*, LBL and LANL HIFAR Group, Edited by D.L. Judd, Lawrence Berkeley Laboratory Report PUB-5123, to be published.

report also details areas where innovative development could significantly reduce the cost of the latter induction units and the overall facility cost. Initial beam experiments on a partial facility could have begun in late FY86 and the facility completed by the end of FY 87.

3. Four-Beam Multiple Beam Experiment (MBE-4)

The MBE-4 is designed to model much of the accelerator physics that we expect to encounter on the HTE, but on a much smaller scale. The MBE-4 will be approximately 12 m long. Measured in units of the initial pulse length, however, it is twice as long as the electrostatic portion of HTE and 2/3 as long as the entire accelerator. This is accomplished by using 0.2 MV cesium in MBE-4 to study the beam dynamics of 2 MV sodium in HTE.

The principal parameters for MBE-4 are set forth in Table I together with the corresponding values for MBE-16 and the reference HTE design for comparison. We note the following with respect to Table I:

(a) The focussing electrode diameter (50 mm) and the beamlet aperture hole diameter (44 mm) are the same as for MBE-16, thereby minimizing the dodecapole harmonic component of the electrostatic focussing field.

(b) Consideration was given to decreasing the transverse dimensions of the focussing arrays but was not done because it would have led to reduced line charge density, λ, which would have foreclosed exploring longitudinal strong-space-charge effects foreseen for HTE.

(c) It should be noted that MBE-4 will be capable of demonstrating significant energy amplification ($\times 4$), current amplification ($\times 4$) and hence power amplification ($\times 16$) — a significant step towards that required for HTE (E$\times$60, I$\times$20).

(d) The accelerating voltage impulses in MBE-4 are relatively large because of the lower injection energy. Effects might, hence, be seen in MBE-4 that would not be significant to the performance of HTE, but their study can provide valuable research results that contribute to the understanding of longitudinal space-charge behavior.

(e) Voltage "ears" will be applied to the head and tail of the bunch to prevent bunch lengthening.

(f) The last entry, $1 - (\sigma/\sigma_o)^2$, is a measure of the space charge defocussing spring constant divided by the mean restoring spring constant and indicates that MBE-4 also addresses the space-charge dominated regime.

Budget constraints dictate that MBE-4 incorporate existing apparatus and components to a large degree. It will be located in the existing Building58 Hi-Bay as shown in Fig. 1. Typical longitudinal cross-sections are shown in Fig. 2. The existing 1 ampere Cesium source which operates reliably at 200 to 400 kV will be converted to four small Pierce sources with alumino-silicate emitter buttons. The matching section will utilize existing probe drives where feasible. Acceleration will utilize existing Astron cores (0.7 volt-second), silicon steel cores (0.9 V s) and Metglas cores (0.1 V s) as well as existing silicon steel tape (0.8 V s) and Metglas tape (0.1 V s) which can be wound into cores as funds permit. The induction insulators will be of relatively inexpensive glass-ceramic. Existing vacuum equipment will be used to a large extent. Existing "lathe-bed" girders from the ERA program will be used as structural supports.

A relative scale comparison of MBE-16 and MBE-4 is shown in Fig. 3.

Table I

Parameter	MBE-4	MBE-16	HTE
Number of beams	4	16	16
Injection energy (MeV)	0.2	2	2
Ion	Cs(K)	Na(Cs)	Na
Injection current/beam (mA)	5(10 max)	150(300 max)	300
Final current/beam (mA)	20(40)	300(600)	6,000
Lattice 1/2-period (m)	0.24	0.33	$\gtrsim$0.3(varies)
Peak gap voltage (kV)	30	250	250
# Accelerating gaps	25	25	$\sim$500
Cores/gap	3	14	—
Length (m)	12	25	450
Length/Injected pulse length	12(5)	3.5(8)	18
Final energy (variable) (MV)	1	8	125
Perveance (K_o) per beam Injection:	4.2×10^{-4}	1.7×10^{-4}	3.3×10^{-4}
Perveance (K_o) per beam Final:	1.2×10^{-4}	4×10^{-5}	1.3×10^{-5}
Minimum value of $\omega_p^2/2\omega_o^2 = (1-(\sigma/\sigma_o)^2)$	0.94	0.94	0.98

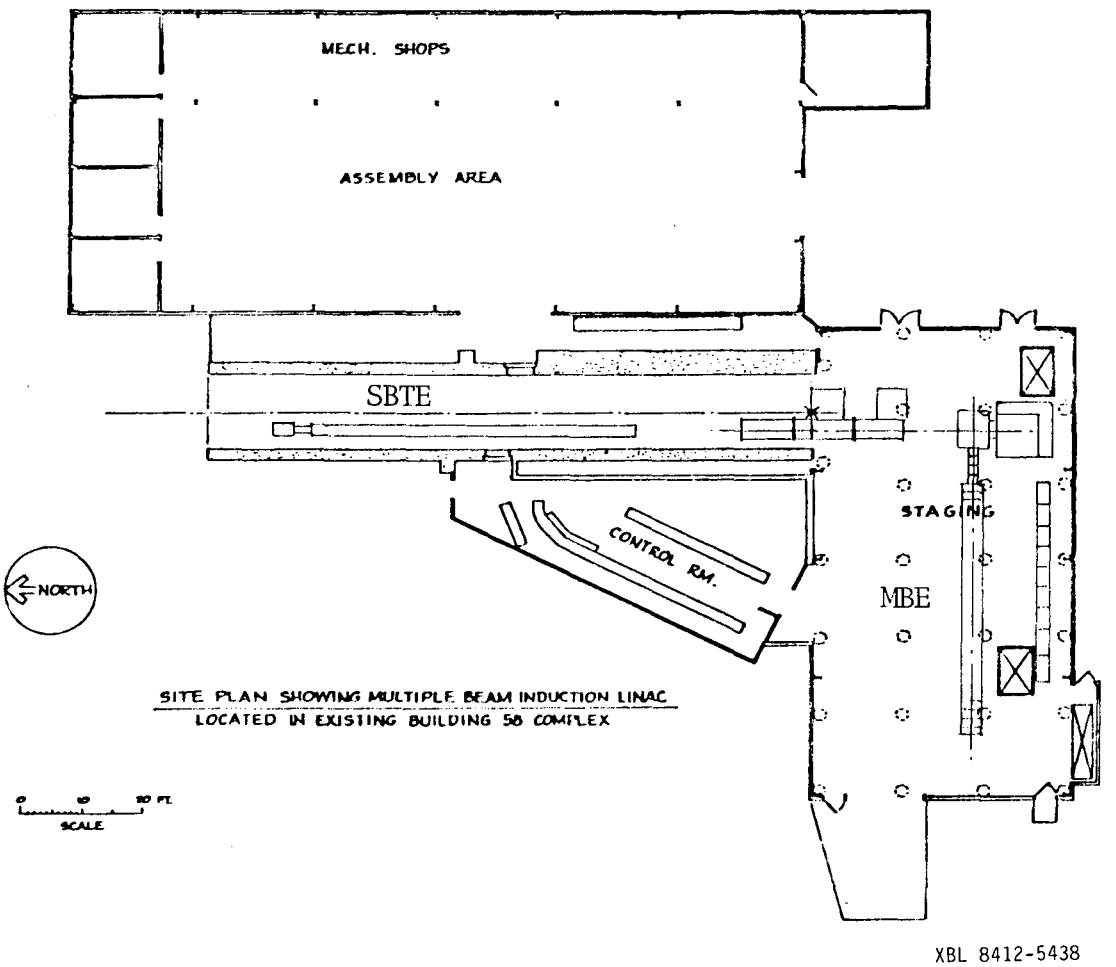

Figure 1. Site plan showing multiple beam induction linac located in existing Building 58 complex.

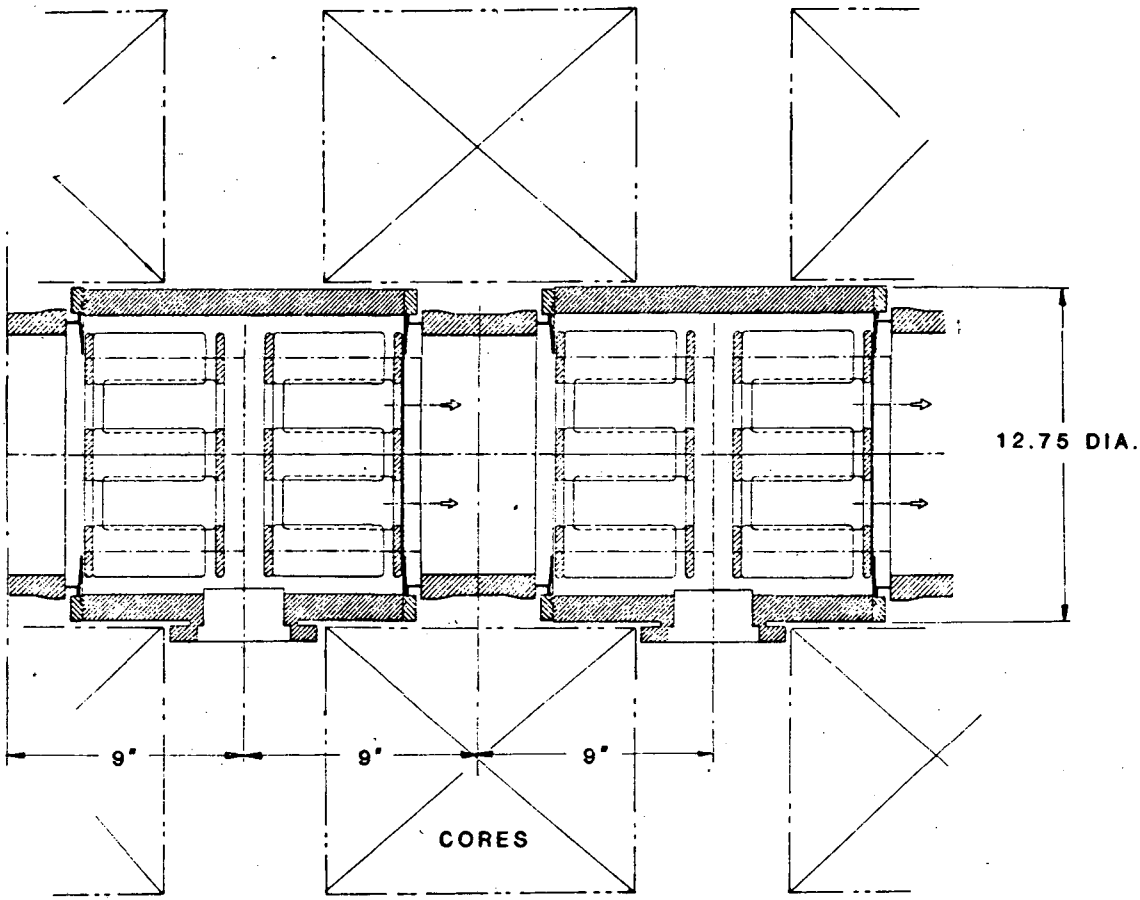

Figure 2. MBE-4 longitudinal cross-section.

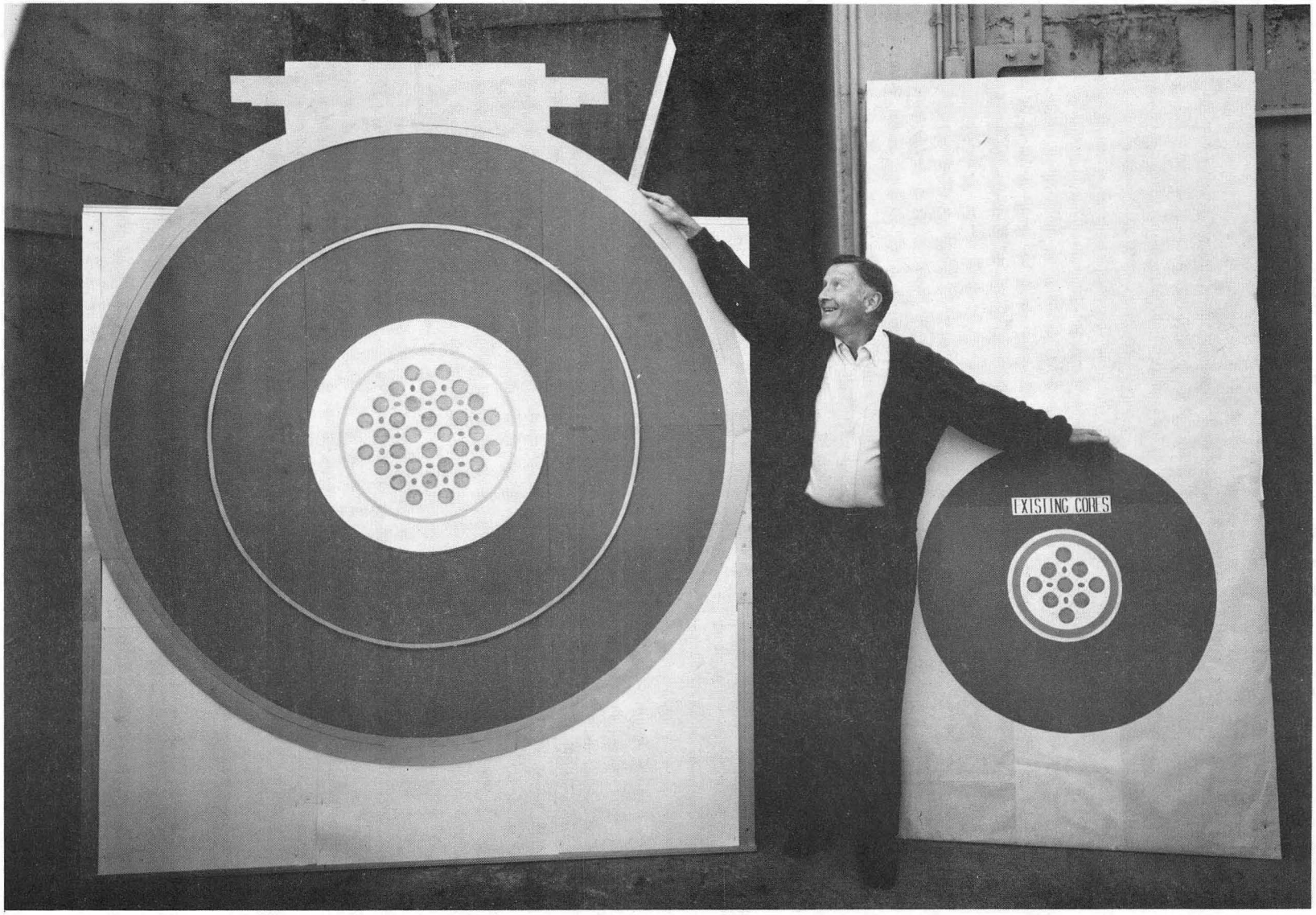

CBB 849-6929

Figure 3. Scale commparison MBE-16 and MBE-4.

Theory

1. Current Amplification in MBE-4 (Kim, Judd, Laslett)

It is evident that when the kinetic energy is to be increased by a substantial factor in a relatively short distance, particular attention must be directed toward the kinematical and dynamical consequences of the discrete acceleration impulses. As already illustrated in the "Revised MBE Program Plan" cited earlier, an interesting method of discretization has been demonstrated (C. Kim) by a computational program based on a similitude algorithm that permits the beam current at any specific location to be independent of time throughout the pulse (presuming constant-current injection). This program, SLID, also provides some useful insight into the dynamical effects of longitudinal space-charge forces, as influenced by variations in the longitudinal charge density.

As with any discretized scenario, the procedure just mentioned necessarily will lead to the development of some saw-tooth variations of particle density along the beam — although the beam may be expected to move rapidly through such a modulation. It is also expected, moreover, that this particular procedure will result in a distinct overall tilt of the charge density *vs.* position at any fixed time, e. Previous computations for a continuous acceleration schedule have been directed (Judd, Laslett), on the other hand, to scenarios such that at any instant the density will remain *strictly independent* of position (in the expectation that this would be desirable), and these scenarios can be discretized in such a way that the overall density tilt remains suppressed. A tilt of particle *speed* necessarily will be present, however, if spatial bunching is to occur.

Some special programs have been developed to permit further comparative investigation of longitudinal space-charge effects in beams subjected to acceleration forces discretized in the different ways mentioned above and also to pursue the associated effect of non-adiabatic changes on the transverse characteristics (esp. envelope radius) of the transported beam. With respect to the abrupt saw-tooth changes of particle density and of speed, one expects that (with any scenario) the *product* λv will not change abruptly (conservation of particle current). With suitable discretization of a continuous acceleration schedule one also may expect to avoid an overall tilt of density versus z at fixed time, but an overall velocity tilt $\Delta v = \ell_0\, dw/dt$ must then be expected if the bunching function

($w = \ell/\ell_0$) is desired to change. As these issues become further clarified, increasing emphasis then of course will be directed to an investigation of the extent to which the theoretically desired wave forms must be accurately synthesized.

2. Transverse Simulation Results (Celata, Smith)

The transverse particle simulation code developed by I. Haber of Naval Research Laboratory was used to study the effect on beam dynamics of (1) nonlinearities of the focusing fields in the 16 beam lattice of MBE-16 or HTE and the 4 beam configuration of MBE-4, and (2) forces due to charge induced on conductors surrounding the beam.

The first of the focusing field nonlinearities considered was the "interdigital nonlinearity," i.e. the field aberrations caused by the imperfect overlap in axial extent of the electrodes. This effect contributes an electrical potential proportional to $r^4 \cos 4\theta$ to the focusing field, plus other terms whose magnitudes are negligible. The sign of the potential alternates from one end of a quadrupole to the other, so that the effect tends to self-cancel. The relaxation code POISSON was used to find the magnitude of this component for the lattices being investigated. This potential, when included in the particle simulation calculations, showed negligible effect on the beam of the interdigital non-linearity, with the beam on or off axis, for half-periods varying between 6 and 12.5 inches and an electrode radius of one inch.

Nonlinearities about the position of a single beam due to the asymmetry of the full electrode array were also investigated. Again the code POISSON was used to determine the magnitude of the nonlinear force for the 16 and 4 beam lattices. The magnitude of the non-linearities was found to be negligible compared to the quadrupole force ($< 0.03\%$ of the quadrupole force for all multipoles but the dipole, which was found analytically to cause $< 4\times10^{-3}$ mm shift of the beam equilibrium position). Therefore investigation using the simulation code was unnecessary. Because of the greater symmetry, non-linear multipole forces for the 4 beam case were somewhat smaller than for the 16 beam case — a factor of about one-fifth, depending on the multipole.

Simulation of the effect on the beam of induced charge on the electrodes showed emittance growth for off-center beams if the tune depression due to space charge was large. For $\sigma_0 = 60°$, $\sigma = 6°$, and a beam centroid oscillation of amplitude $\Delta x = \Delta y = 2.75$ mm, the emittance was observed to grow by 30% in 75 periods, with superimposed oscillations up to 70% of the initial emittance. For the same conditions and $\sigma = 12°$, no growth was seen. It should be noted that in the code, unlike the actual experiment, the conductors are assumed to be present at all values of z, the longitudinal coordinate. Thus the simulation results give an upper bound for this effect. The emittance growth seen consisted of beam heating, with only a small oscillation in the beam size occurring.

The growth in the emittance had superimposed on it the above-mentioned oscillations, in a pattern which seemed to indicate an oscillation with frequency slightly above σ_0 beating with an oscillation at the coherent betatron frequency. Phase plots indicated the mode present to be an odd multipole — possibly the sextupole mode. Analytical theory, extended by numerical work, using the linearized Vlasov equation, induced charge forces for a round pipe, and the KV distribution was then used to demonstrate that the third order mode can be driven by a coherent betatron oscillation when the tune depression is large. For low σ,

the frequencies of these two modes are nearly equal, giving the beating phenomenon seen in the simulation results. The frequencies seen in the simulation agreed well with the analytical results. The analytical theory indicated that the perturbation potential was proportional to $[\omega_o^2(\Delta x)^3 a^3]/b^4$, where a = beam radius, b = pipe radius. Though the simulation shows qualitatively the same behavior, the quantitative dependences have not yet been compared.

This emittance growth due to induced charge appears to limit the lowest value of σ available to experiment. Investigations are presently under way, using the simulation, to try to determine the mitigating effect of shrinking the electrode radius, thus moving the conducting surfaces farther from the beam. This will cause a greater dodecapole field contribution, which was shown in the last annual report to have deleterious effects on beam emittance. Since the induced charge effect is predicted to fall off quickly ($\sim b^{-4}$), however, it is hoped that some trade-off is possible.

Finally, work is in progress to adapt the simulation to study the effect of source non-uniformity on the transverse beam emittance.

3. Longitudinal Phenomena in MBE and HTE (Bisognano)

Longitudinal space charge phenomena on an induction linac bunch are characterized by a single parameter, v_p, the velocity of the space charge wave. For example, the evolution of a velocity perturbation v is determined by the ratio, v/v_p, with time scaled as the ratio of the length of the perturbation to v_p. If $v/v_p \gg 1$, the propagation is ballistic; for $v/v_p \ll 1$, the propagation is space charge dominated. Bunch lengthening also proceeds at the space charge wave velocity. A primary goal of possible multiple beam experiments (MBE) is to address the longitudinal physics of the High Temperature Experiment (HTE). Although particle species, current, number of beamlets, bunch length, and transport distance are quite different between the MBE and HTE, the simple, single parameter scaling of longitudinal phenomena discussed above allows the MBE, through judicious choice of these parameters, to address much of the longitudinal phenomena which pertain to the HTE.

An induction linac ion beam will experience discretized acceleration in passing through the finite array of induction module gaps. This process can introduce steep velocity variation on the bunch which if not smoothed by space charge can lead to large linear density spikes. Particle simulation results indicate that when the induced velocity perturbation v satisfies the condition $v/v_p < 1$, there is space charge smoothing. For the HTE this condition corresponds to step voltages of about 15 KV. From wave velocity scaling, MBE experiments with 5 mA per beamlet will behave comparably with 1 kV steps. Larger voltage steps or lower currents will address the onset of strong density variation. Another issue of importance in the HTE is the requirement of longitudinal end focusing to compensate for space-charge induced bunch lengthening. Without such focusing, an HTE bunch will lengthen by a large fraction of the bunch length. For obtainable currents and bunch lengths in MBE designs it is found that similar behavior can be achieved, although the transport distance is an order of magnitude smaller. As these examples indicate, proper choice of beam parameters with regard to scaling allows modest multiple beam experiments to investigate the longitudinal physics which will be encountered in the High Temperature Experiment.

4. High Temperature Experiment-System Model (Lee)

To guide the choice of major parameters for the High Temperature Experiment (HTE), a simple model of the target, final focus, and accelerator system has been devised. The underlying goals of HTE should be realized at a minimum cost, i.e. heating a solid density target to temperatures in range 50–100 eV, and providing a basis for the evaluation of a driver technology. These goals are reflected in the choice of ion mass (A) and energy (E), pulse length (ΔT), current (I), and the number of simultaneously accelerated beamlets (N). The target model takes into account the principal processes involved in energy deposition and loss which are also expected to be present in a fusion pellet. The accelerator system model incorporates the main driver features of high brightness source, electrostatic and magnetic focussing, and acceleration limits due to maximum gradient, core mass and velocity tilt. Current limits are imposed in the final compression and focus zone and they connect the target and accelerator models.

In order to reach a desired final temperature (T), beam irradiance must be selected to balance the black body emission rate ($\propto \sigma T^4$). It is also necessary to supply the specific energy to the target required to reach temperature T; to do this the pulse length is set proportional to $RT^{3/2}/N$ where $R \propto E^{3/2}/A^2$ is the particle range. Two constraints are applied at this point. First, the range must exceed the value .004 gm/cm^2 because stripping of electrons would be otherwise very incomplete and deposition would not be similar to a fusion driver. Second, the pulse length must not be so great that the target disassembles during heating. These constraints effectively limit the available parameter space (E,A) to an oblique band for given temperature (see Fig. 4).

A third constraint which restricts E and A is the allowable perveance per beamlet in the final focus. This is a limit on the line charge or current which can be *precisely controlled* and *focussed.* At present the best estimate for this limit in the context of HTE is

$$K_o = \frac{2\, I_o\, Z^2}{\beta^3\, A(31\times 10^6\ \text{Amp})} < 2\times 10^{-4}\ .$$

where I_o = particle beam current (part-amps). The resulting boundary in the (A,E) plane is shown in Fig. 4. For given T,N and spot size r, the particle energy must lie above a critical value which is only weakly dependent on A ($E_{crit} \propto A^{-2}$). The minimum cost accelerator has parameters on this critical line.

An accelerator model is used to estimate the system length (and ultimately its cost). For high values of A the required beam pulse length is very short and the accelerator length is largely determined by the maximum allowable gradient ($\sim$ .5 MV/m). For low values of A the pulse length is long and acceleration must be at a much reduced rate to avoid an unacceptable concentration of core material. The high mass option appears to be the cheaper one at present, with 140 MeV K^+ ions providing a good match to 80 eV final temperature in Al.

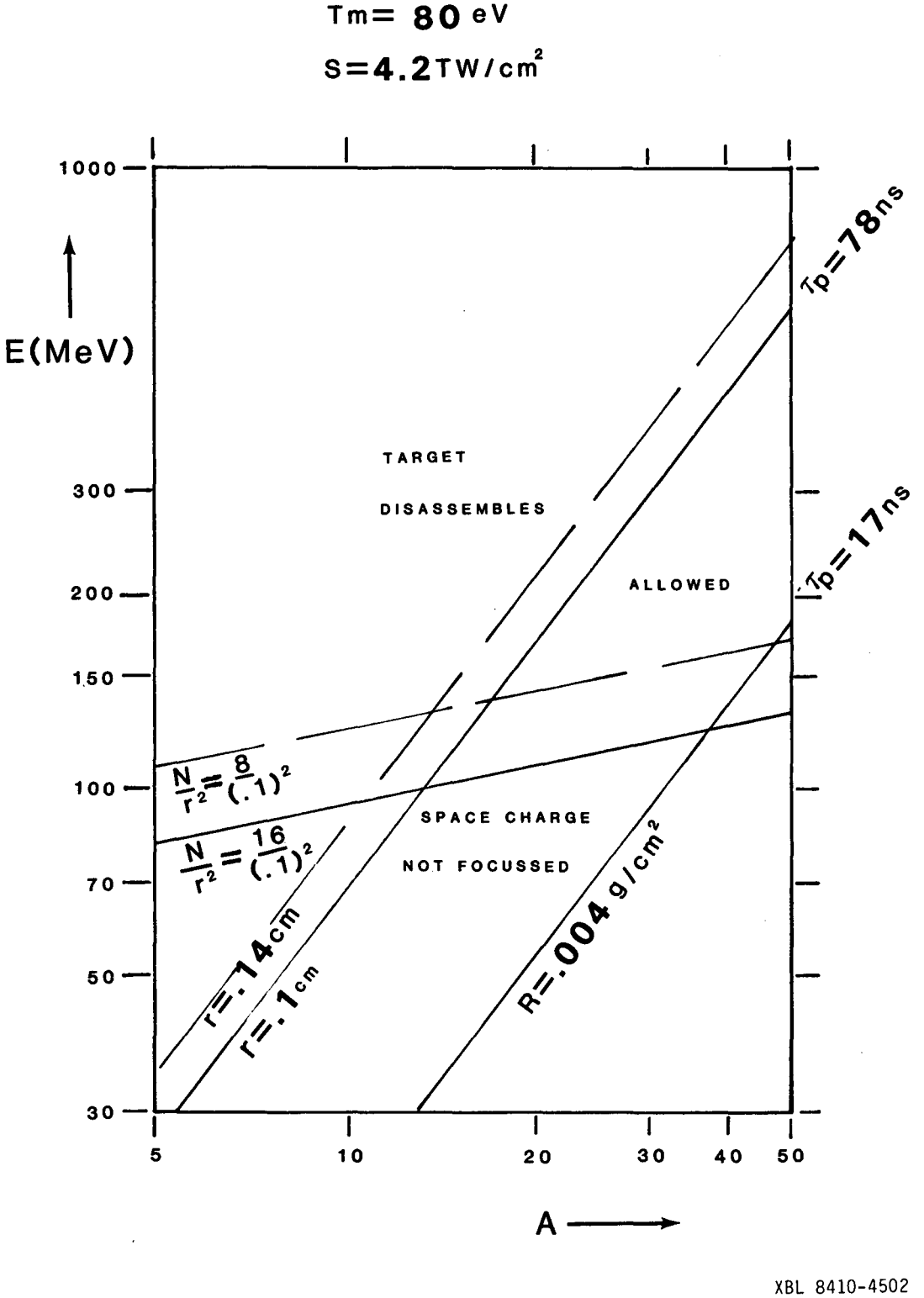

Figure 4. Energy and mass number boundaries for an Al target heated to 80 eV. The high A are excluded by shortness of range, low A are excluded by target disassembly, and low E are excluded by the perveance condition.

Single Beam Transport Experiment

1. Transverse Focusing Experiment (Tiefenback)

A portion of this reporting period was devoted to realignment of the quadrupole lattice, addition of some diagnostics tools and liquid nitrogen-cooled cold traps for pumping water vapor. A second deep gridless Faraday cup was added to the diagnostics. This cup is of the same design as the one at the lattice exit (Q80), but placed after the matching section (Q1). The ability to move the first doublet of quadrupoles of the regular lattice horizontally in a controlled fashion (to induce deliberate beam misalignments) was incorporated at the same time. In addition, the entire ion gun assembly was mounted on a gimbal setup, movable from outside the vacuum chamber, to aid in fine alignment of the beam in the lattice. The capability to offset the beam in the lattice was desired for the purpose of checking the importance of this effect in a real lattice.

Simulations recently run for intense beams including induced charges in the focussing lattice, beam misalignment and consequent image charge asymmetry predicted significant emittance growth. No effect larger than usual measurement variation has been seen so far, but misalignments used to date have been limited to those causing only a few percent beam loss (3–4 mm maximum offset). The measurement of this effect is not yet complete.

The vacuum upgrade with the cold traps results in a factor of 4–5 decrease in pressure, as measured with a shielded ion gauge. Ultimate pressure now is about 1.0×10^{-7} Torr, versus 5.0×10^{-7} Torr previously. This low pressure assures us that less than 1/2% of the beam will undergo charge-state-changing collisions with the background gas. Such collisions could have caused spurious effects that might have implied emittance growth.

The regular program of beam measurements to map out the instability boundaries is proceeding. As reported earlier, no limiting value of the depressed phase advance per period, σ, could be identified, at least down to $\sigma = 8°$, provided σ_o held below 90°. Above 90°, however, we have identified bands of stability (σ_o,σ), for our conditions corresponding to (90°,20°), (100°–50°), and (120°,90°). The work is ongoing and should be finished early in FY 85.

2. Longitudinal Beam Experiments (Faltens)

In addition to the transverse focusing experiments for which they were designed, the SBTE and 1A Cs injector both provide an opportunity for performing longitudinal physics experiments such as bunch compression, bunch end control, and studies of the propagation of charge and velocity disturbances. The latter can range from the single particle regime at low beam intensities to the space charge wave regime at high beam intensities. A few such exploratory experiments were performed on the well instrumented SBTE beam and are reported here.

In the absence of longitudinal focusing, the bunches elongate from space charge repulsion (and, in the process, undoubtedly receive energy modulations which cannot yet be measured). The characteristic bunch lengthening due to space charge is shown in Fig. 5(a), in which the approximately 4 μs rise and fall times of the bunch are due to two effects: an elongation of each end and a recoil pulse traveling into the bunch, each of which happen to account for about 2 μsec (1 meter spatially after a 13 meter travel distance): of the 4 μsec ends. The transport measurements given elsewhere in this report are always performed on the undisturbed interior portions of the bunch. To decrease the bunch elongation and the generation of inward traveling space charge waves requires the application of longitudinal fields of about 5 kV/m at each end of the nominally 120 keV, 16 mA, 1/2 μs rise-and-fall Cs^+ beam which emerges from the gun-plus-matching-section. Note that at low beam intensity, Fig. 6(b), the current risetime after 13 meters travel is much shorter than that of the full intensity beam.

There are several possible ways to achieve bunch length control such as inserting a few low-voltage induction acceleration cores at the junctions between transport section vacuum tanks, or by using the beam-enclosing quadrupoles as drift tubes by superimposing a common-mode pulse voltage on top of the $\pm$ DC focusing voltages. A very imperfect focusing method — but one that shows the effect — is to superimpose the focusing "ear" on the gun voltage. This was done by making the ground lead of the source Marx the secondary of a small pulse transformer, through which fast pulses could be applied at any time during the gun voltage pulse. The focusing effects of a small positive pulse at the rear of the bunch or a small negative pulse at the front are shown in Figs. 5(a) and 5(b).

The marked difference in the propagation of identical disturbances on a high intensity and a low intensity beam is illustrated in Figs. 6(a) and 6(b), where the beam intensity was attenuated by a factor of 30 downstream of the disturbance.

The remaining experiment of this exploratory series will be to show overall bunch compression. Calculation and computation show that a modest velocity ramp will lead to a 1.6$\times$ current amplification in the center of the bunch and practically reach the maximum current possible in the available aperture. This will require superimposing a 7% cosinusoidal pulse of 12μsec period onto the nominally square gun pulse.

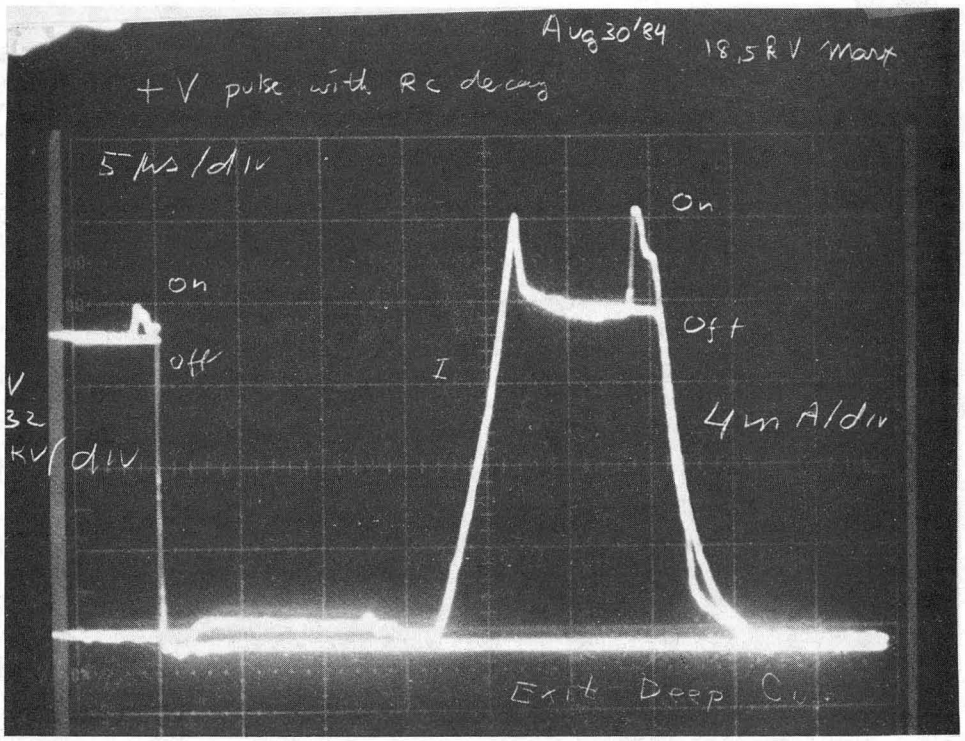

Figure 5(a). Gun voltage, left, and bunch current, right, with and without positive ear at tail of pulse.

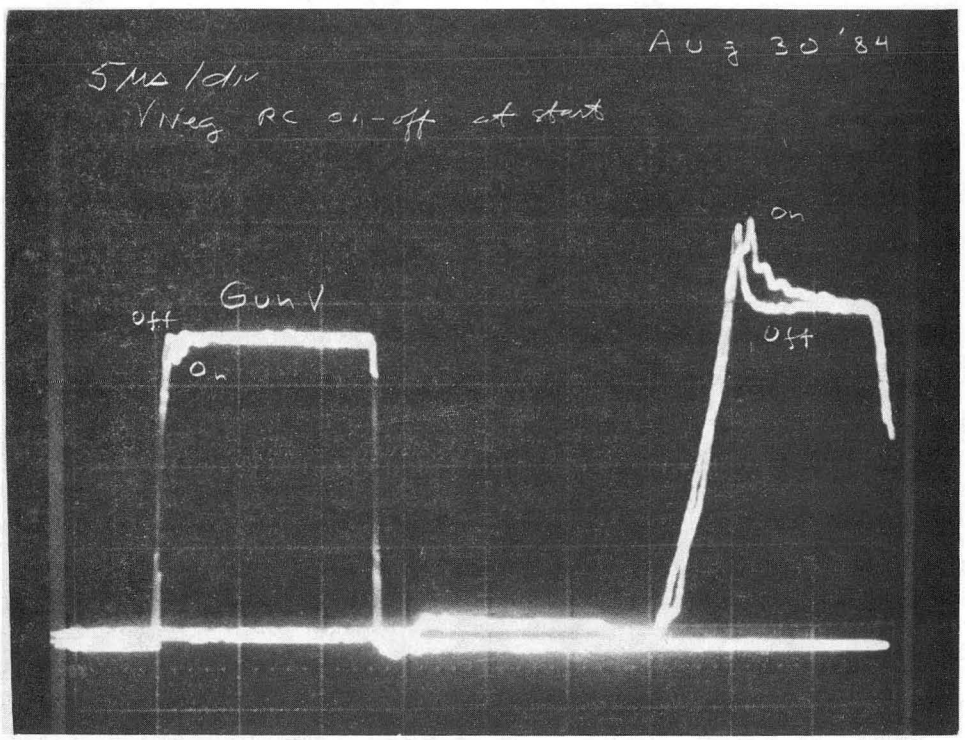

Figure 5(b). Gun voltage, left, and bunch current, right, with and without negative ear at front of pulse.

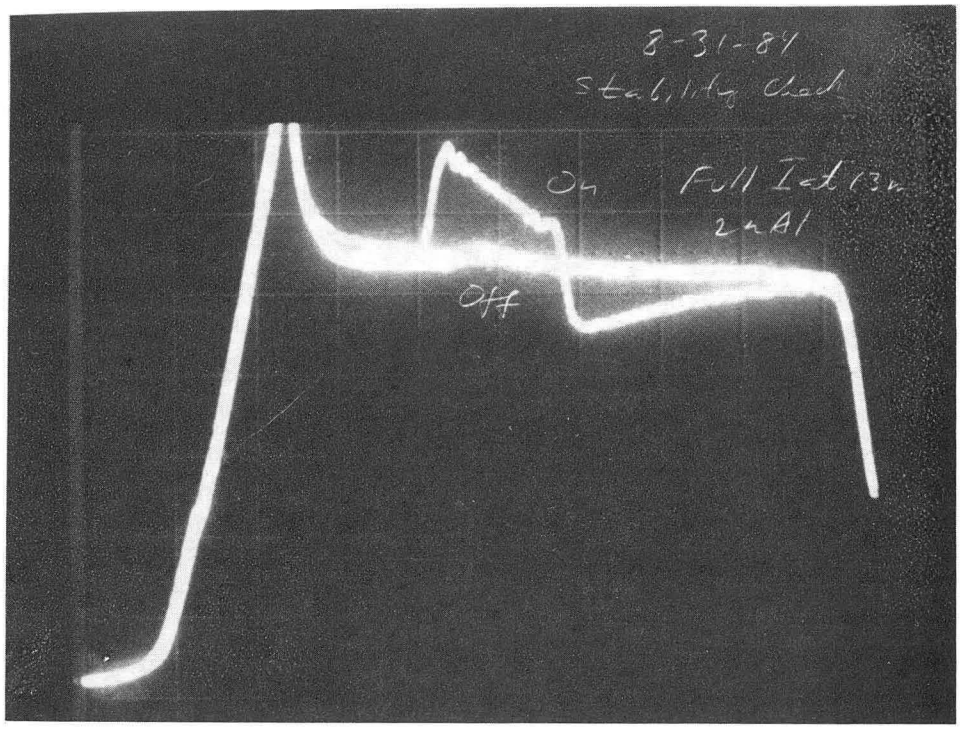

Figure 6(a). Positive voltage perturbation, off and on, on high intensity beam. 2μs/div.

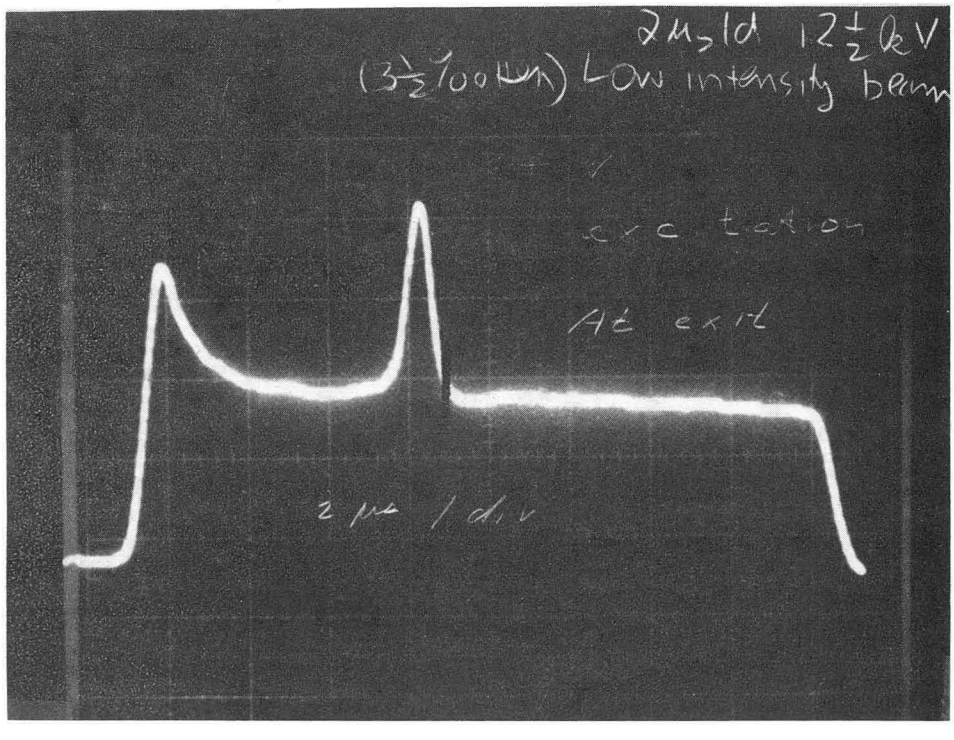

Figure 6(b). Positive voltage perturbation on low intensity beam.

Neutralized Beam Focusing Experiment

(Krafft)

The main experimental result during the reporting period was that superior beam neutralization has been achieved using a hot wire electron emission source. In this method electrons are emitted thermionically into the beam volume from tungsten filaments heated to about 2500°K. Experiments show that to obtain this superior neutralization, it is necessary that the filaments intercept the ion beam.

Electron emission occurs only when unneutralized space charge fields are present. Emission proceeds until the space charge is cancelled to a large degree. The final line neutralization was measured experimentally to be equivalent to that of a uniform beam with fractional neutralization

$$f = .995$$

The results of a measurement of the space charge potential surrounding the neutralized beam is shown in Fig. 7.

The better neutralization has not resulted in significant improvement of lens performance. Consequently a program of PIC simulation has been initiated so that improved understanding of the lens is possible. The goal of this work is to calculate the self-consistent electric field when thermal effects of the electrons are included. Various regimes are to be studied with particular emphasis on the experiment. A preliminary result is that large non-linearities are present in the self-consistent electric field which degrades the quality of the lens. When simulation noise levels have been reduced to suitable levels, detailed comparisons with the experiment will be made.

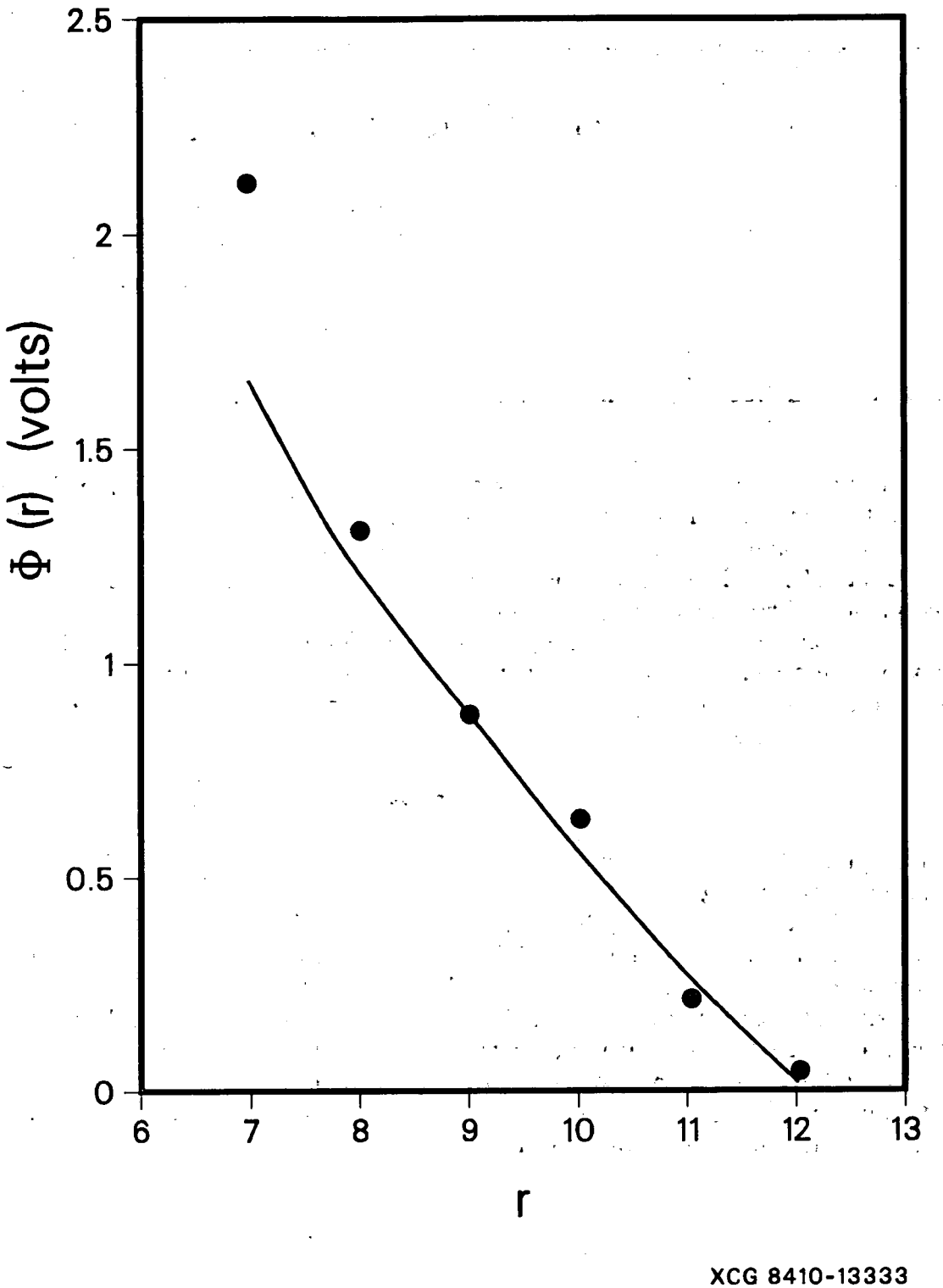

Figure 7. Space charge potential outside beam as a function of position. $T_F = 2400°K$ B = 0.

Range Energy Measurements

1. Range-Energy Relation for Heavy Ion Inertial Fusion - (H.R. Bowman, H.H. Heckman, Y.J. Karant, J.O. Rasmussen, A.I. Warwick and Z.Z. Xu*)

Of critical importance to the problem of ion-target coupling for Heavy Ion Fusion (HIF) is the range-energy relation of heavy ions in (cold) matter. A unique feature of heavy ion beams for HIF, E/A $\leqslant$ 150 MeV, is the very low charge state at which they will be accelerated. Such beams, upon penetrating the target, will have ionic charge-states far from the equilibrium values characteristic of their velocity β and the target material. As a consequence, both the rate of energy loss, dE/dx, and the effective charge Z* of the incident heavy ions in matter will be initially low, the latter increasing to their equilibrium values as electron-stripping takes place. The effects of diminished dE/dx and Z* will tend to increase the range of the ions in the target.

Bevalac experiment #730H is being carried out to obtain range-energy data pertinent to HIF by measuring the range-energy for Au ions, E/A $\leqslant$ 150MeV, accelerated and incident on CH and Au targets at charge states Z_{accel} = 12, 32 and 61. A crucial aspect of this experiment is the availability of low-charge state, high-rigidity beams of heavy nuclei at the Bevalac.

The first phase of the experiment was performed at Beam-40 in July 1984, using $^{+61}$Au beams at E = 150 A MeV and 50 A MeV to establish the (charge-equilibrated) energy-loss rates and ranges of these ions in high- and low-Z target material. The experimental techniques used in these measurements involved:

1) Beam velocities by time-of-flight (TOF), with $\delta t \sim 200$ ps over a 20 m flight path.
2) dE/dx by measurements of ΔE(TOF) vs. foil thickness Δx.
3) Integral ranges by use of visual track detectors and circular, wedge shaped absorbers.
4) Charge spectra of Au beam, $Z_i(\beta)$ by use of the Beam-40 0°-magnetic spectrometer.

*Fudan University, Shanghai, China.

Figures 8 and 9 give our direct observations of the range and dE/dx versus energy per amu under equilibrated conditions. The data are preliminary in that, although small, systematic corrections and refined TOF calibrations will be implemented as the experiment proceeds. The range data shown in Fig. 8, when fitted to least-squares polynomials (not shown), exhibit dispersions of σ = 1.2% (Au) and 1.9% (CH), dispersions that include all statistical and systematic errors attributable to the velocity and range measurements and TOF calibrations.

The experimental results are compared with the ranges and dE/dx predicted from calculations using computer code of Benton and Henke,[6] which is based primarily on the proton range-energy relation given by Barkas and Berger[7] and the heavy-ion range data ($E/A \leq 10$ MeV) of Heckman et al.[8] The values of the ionization potentials for CH and Au used in the calculations were $I_{adj.}$ = 63.2 eV and 7967 eV, respectively.

6. E.V. Benton and R.P. Henke, Nucl. Inst. and Methods, 67, 87 (1964).
7. W.H. Barkas and M.J. Berger, NAS-NRC Publ.-1133, 103 (1964).
8. H.H. Heckman et al., Phys. Rev. *117*, 544 (1960).

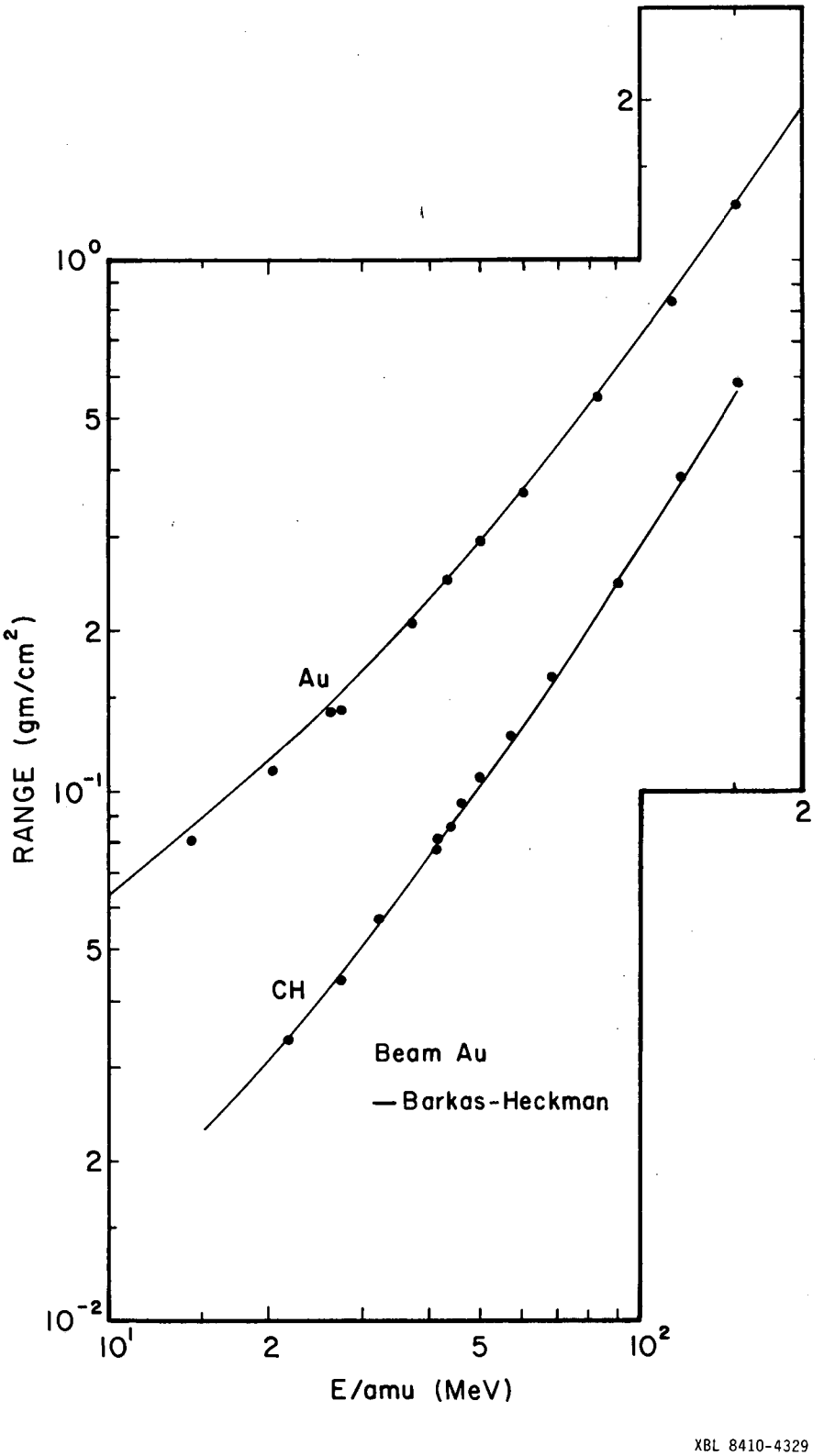

Figure 8. Range-energy relation for Au ions in CH and Au. Data are preliminary. Curves are based on scaling of the proton range-energy relation and the range-extension of heavy ions due to charge neutralization.

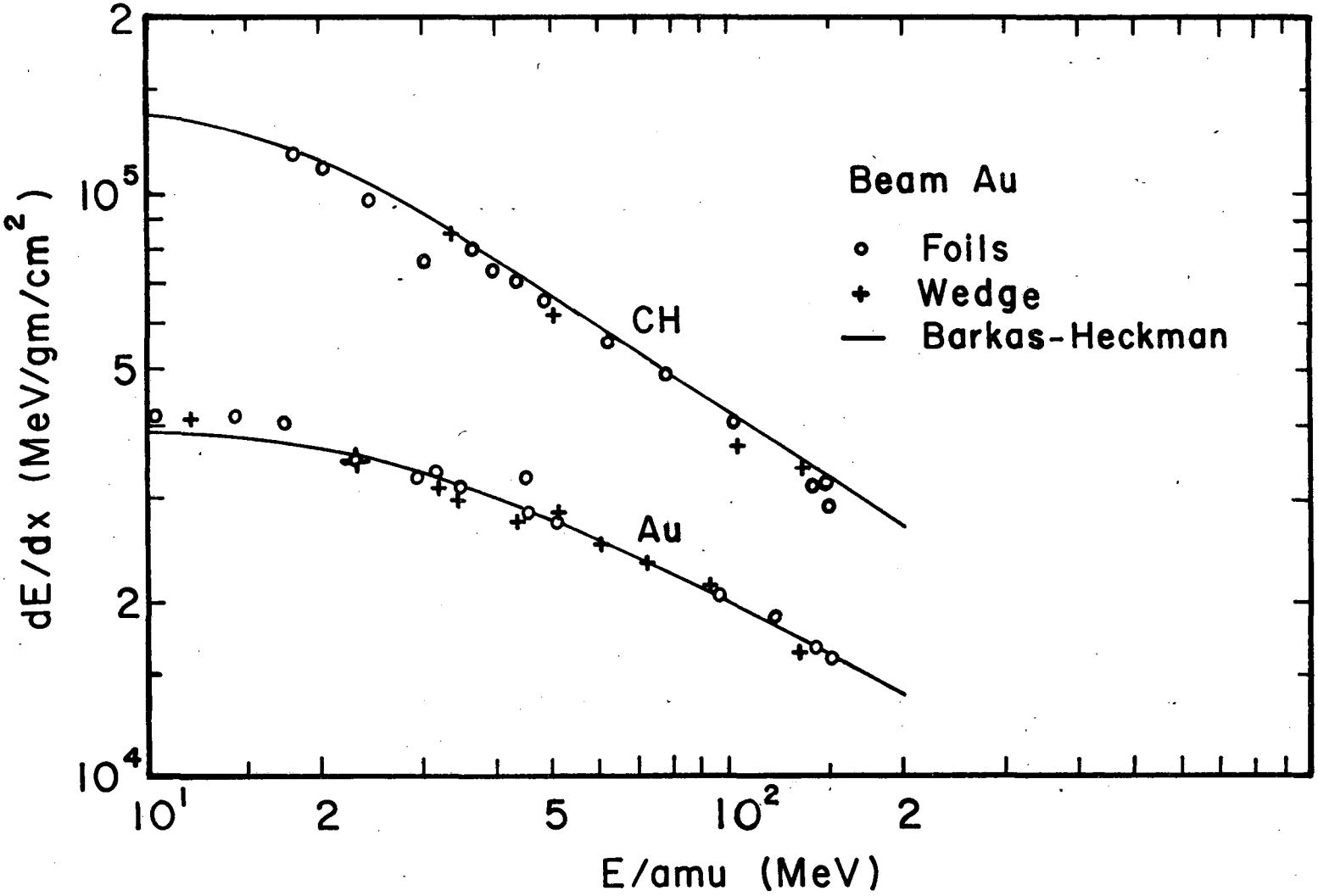

XBL 8410-4328

Figure 9. Measured energy-loss rates of Au ions in CH and Au. Data are preliminary. Curves are described in Figure 8.

Source Development Work

(Warwick)

1. K^+, $Na,^+Cs^+$ Emission from Alumino Silicates

A fabrication technique has been developed by which alumino-silicate emitters can easily be made. Na^+, K^+ and Cs^+ emitters have been made by this technique and their emission limits measured.

The appropriate alumino-silicate is cemented to a heater can at room temperature. Larger area sources can be made repeatably by this method, which is more convenient than alternative melting techniques. These emitters have essentially the same emission limits as those made by melting material on the heater face; first tests indicate that the emittance is somewhat higher. Figure 10 shows a comparison of emission current density versus voltage on a test diode for K^+, Na^+ and Cs^+ ions. The straight lines are the calculated space charge limits. As the thermal limit is reached (for Na^+ and K^+) the emission falls below the space charge limited value. These curves are typical; between local points on the emitter the emission limit may vary considerably. Thus non-uniformity of emission is apparent at values of the average current density lower than the limits shown here.

2. A Candidate Design for MBE-4 Cs^+ Injector

During the coming year it is planned to build the first part of MBE4, consisting of gun, matching section and some acceleration. The progress in designing the ion source, gun and matching section is described here.

2.1. Ion Source

The most convenient source to operate is a Cs^+ alumino-silicate emitter. One such source, 5 cm^2 in area, operates on SBTE with a normalized emittance

$$\pi \epsilon_N = 1.5 \times 10^{-7} \pi \text{ m rad}$$

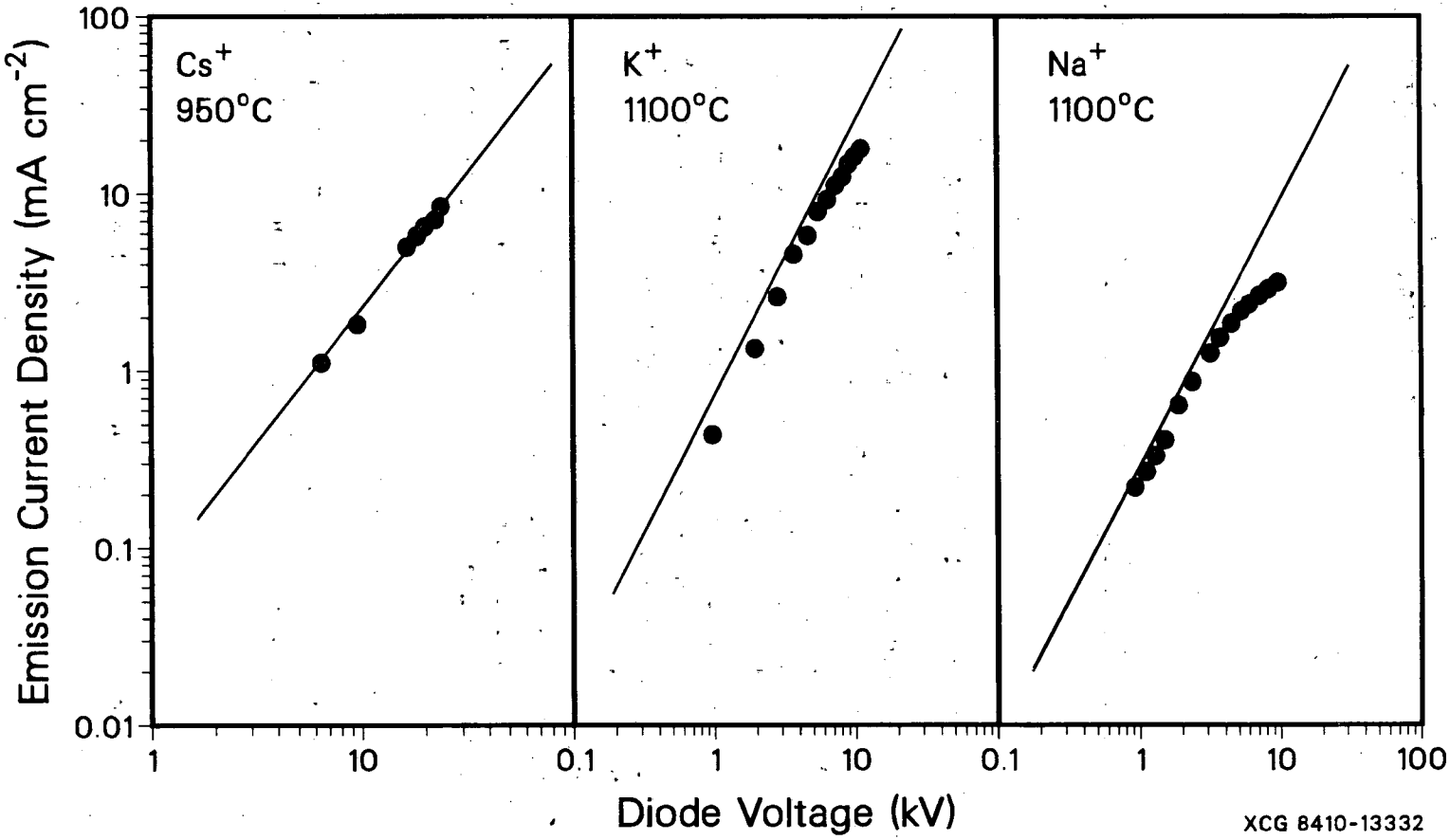

Figure 10. Emission current density limits for alumino-silicate sources of alkali ions.

The candidate gun design for MBE-4 requires four such sources, each of larger area (10 cm^2). Figure 11 shows results from a Cs^+ emitter made by the technique outlined in Section 1. This emitter was installed in SBTE and its emittance was measured at an emission current density of 3.2 mA cm^{-2}. The result was

$$\pi \epsilon_N = 2.7 \times 10^{-7} \pi \text{ m rad}$$

six times the thermal value and almost twice that of the standard SBTE source, which is made by a more difficult technique of melting alumino-silicate onto the heater can. It indicates what can now be achieved easily and reproducibly for larger area emitters. In the design for an MBE4 gun, discussed below, this emittance scales to about

$$\pi \epsilon_N = 2.0 \times 10^{-7} \pi \text{ m rad}$$

for a 5 mA beamlet at 200 kV. The validity of this result needs further scrutiny, aberrations in SBTE may be contributing to the measured emittance. Figure 12 shows measured rms emittance angles as a function of current density. These data were obtained in a simple test diode, relatively free of aberrations. At 3 mA cm^{-2} of Cs^+ emission this result shows an rms angle of twice the thermal value, suggesting that lower emittance may be obtainable from a carefully designed gridless gun.

2.2. Gun Optics

An optics design has been evolved with engineering simplicity as a high priority. Each beamlet is a single gap diode, shown in Figure 13. The shaped anode produces convergent rays, somewhat aberrated, which pass through a hole in the ground plane plate where they are defocussed into a slightly divergent beam. Breakdown limits are not violated, the gun should be good up to about 400kV and the beamlet does not pass through any grids. At 200 kV, the nominal operating voltage, this gun will produce about 20 mA of Cs^+ which will be collimated to the required 5 or 10 mA, reducing both aberrations and emittance in the process. Figure 14 shows the beam characteristics. An aperture of 0.5 cms radius is required to obtain 5 mA at 200 kV. Further study is needed to determine the sensitivity of this open design to the metal vacuum envelope and support structures.

2.3. Gun Layout

The MBE-4 gun will be mounted on the column of the 500 kV Marx. Each alumino-silicate emitter will be individually heated and the entire gun mounted as a unit on the Marx tank/column. This allows checking of alignment. The aperture plate which defines the beam position is part of the matching section assembly so that alignment between gun and matching section are not critical. Furthermore, the collimated beams are precisely positioned as they enter the transport structure and a fourfold electrostatic steering device as the first transport element will be sufficient to align the beams completely.

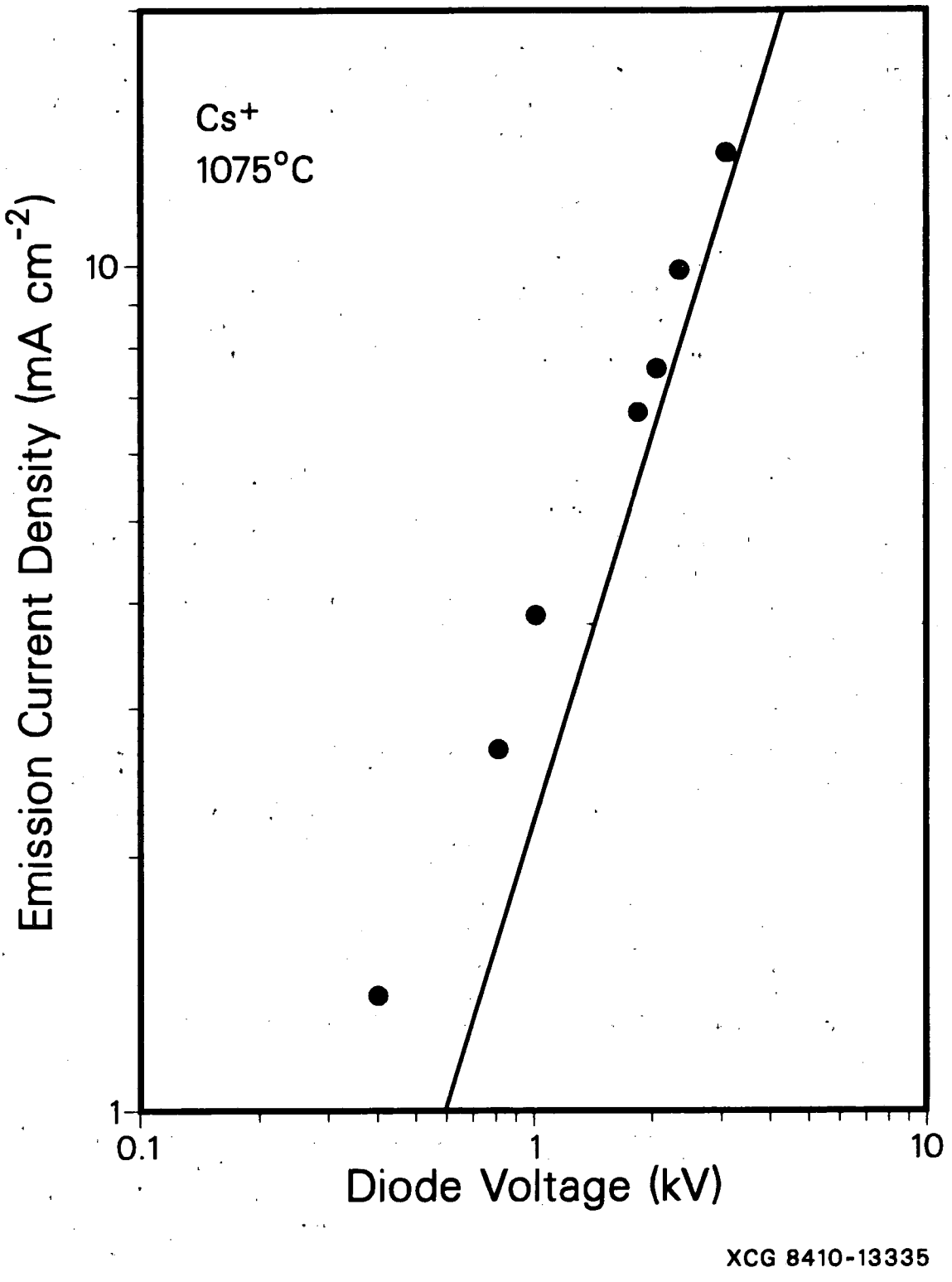

Figure 11(a). Emission from a Cs^+ alumino-silicate. The straight line is the Child Langmuir prediction ($V^{3/2}$) for a planar diode with a somewhat uncertain normalization.

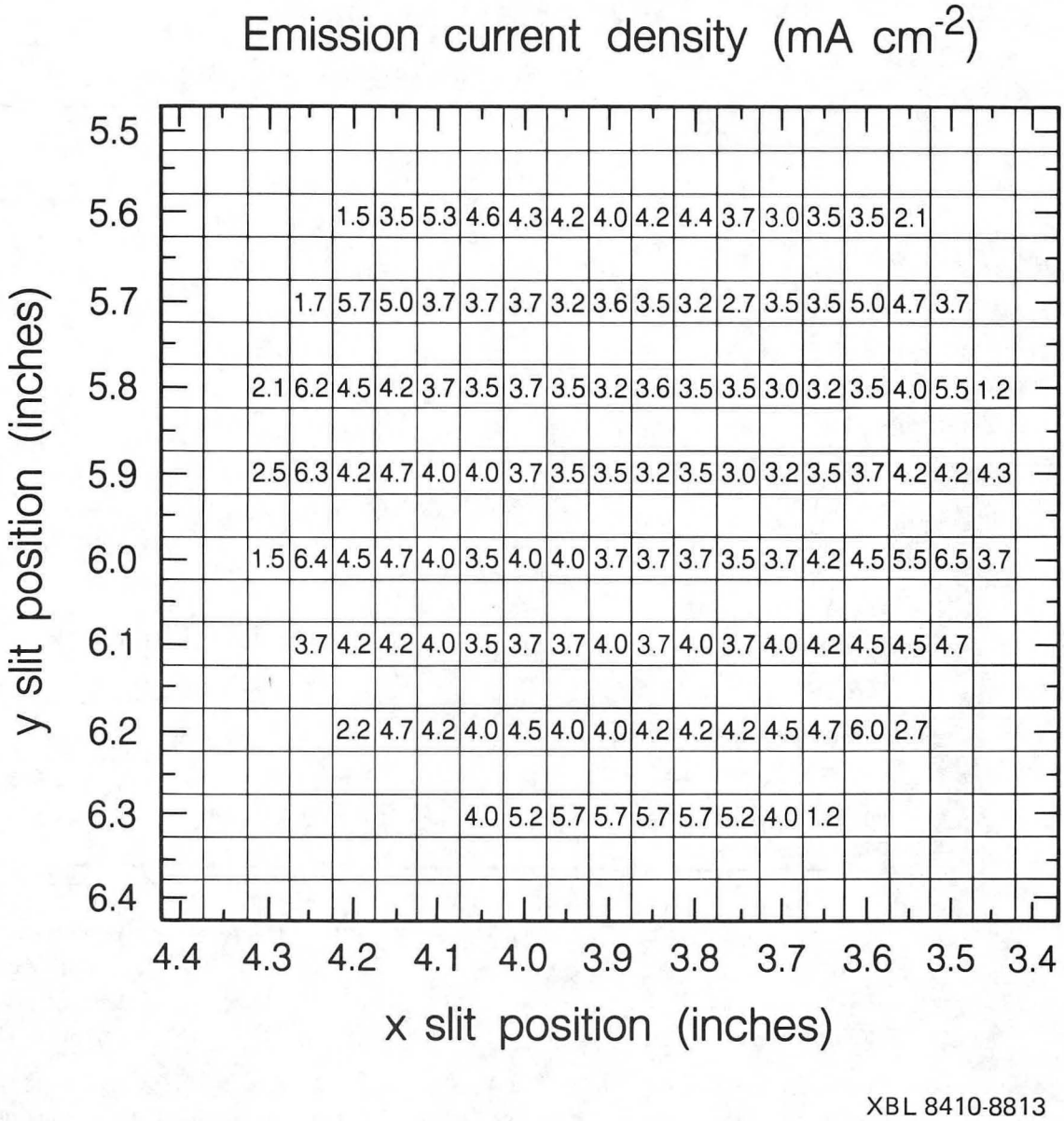

Figure 11(b). Emission uniformity from a Cs^+ alumino-silicate source.

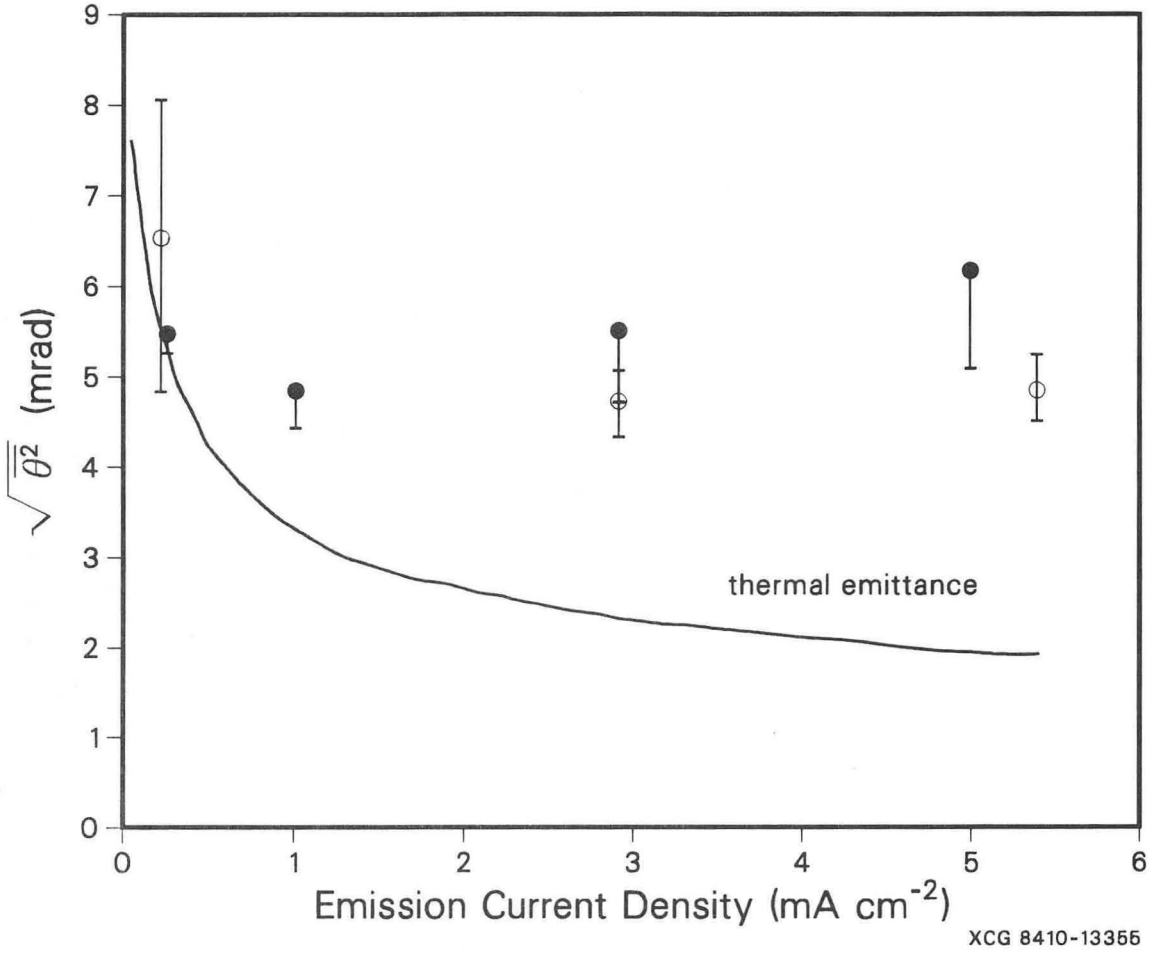

Figure 12. Emittance angles versus emission current density from a Cs^+ aluminosilicate.

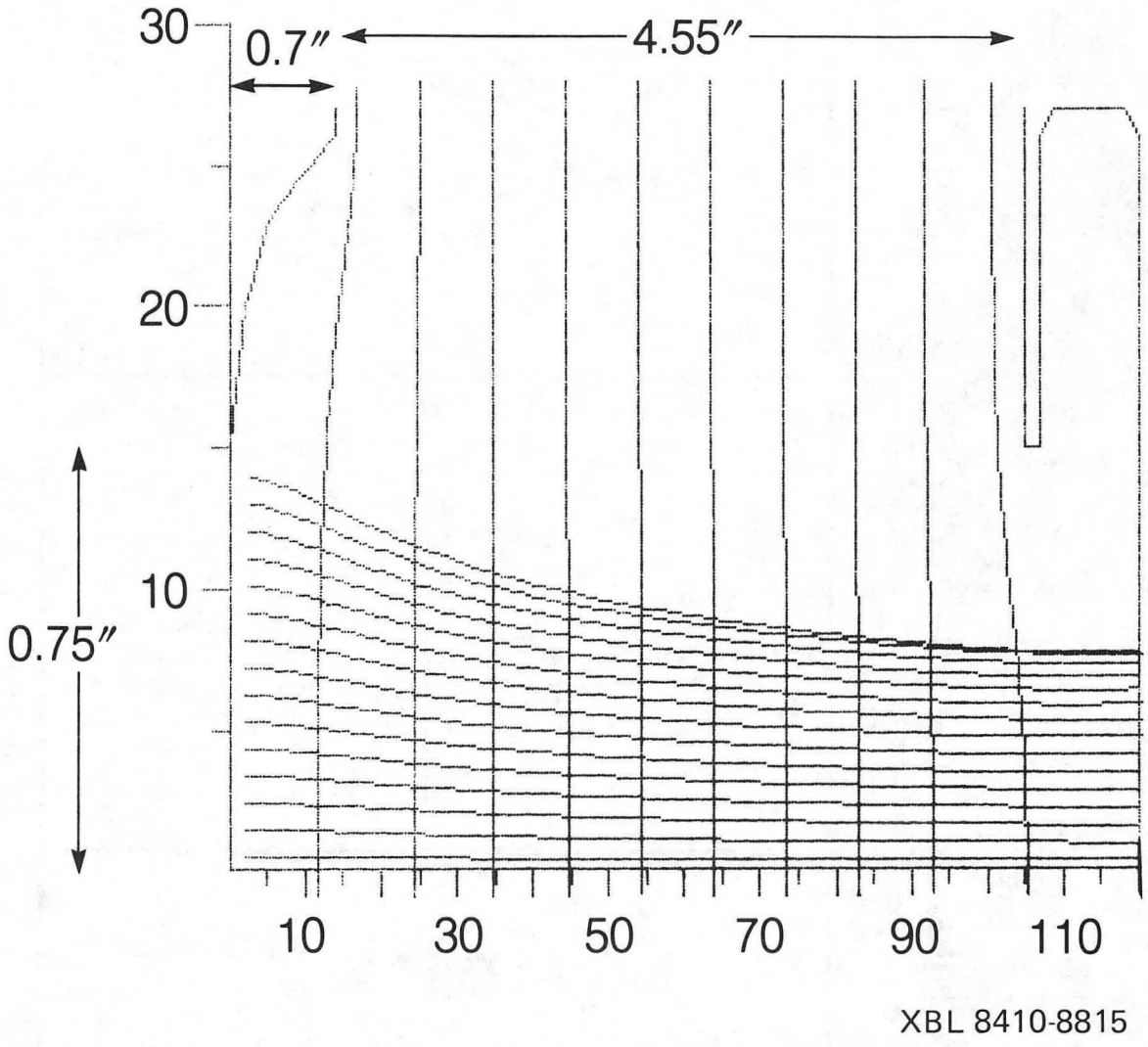

Figure 13. Optics design of MBE-4 diode.

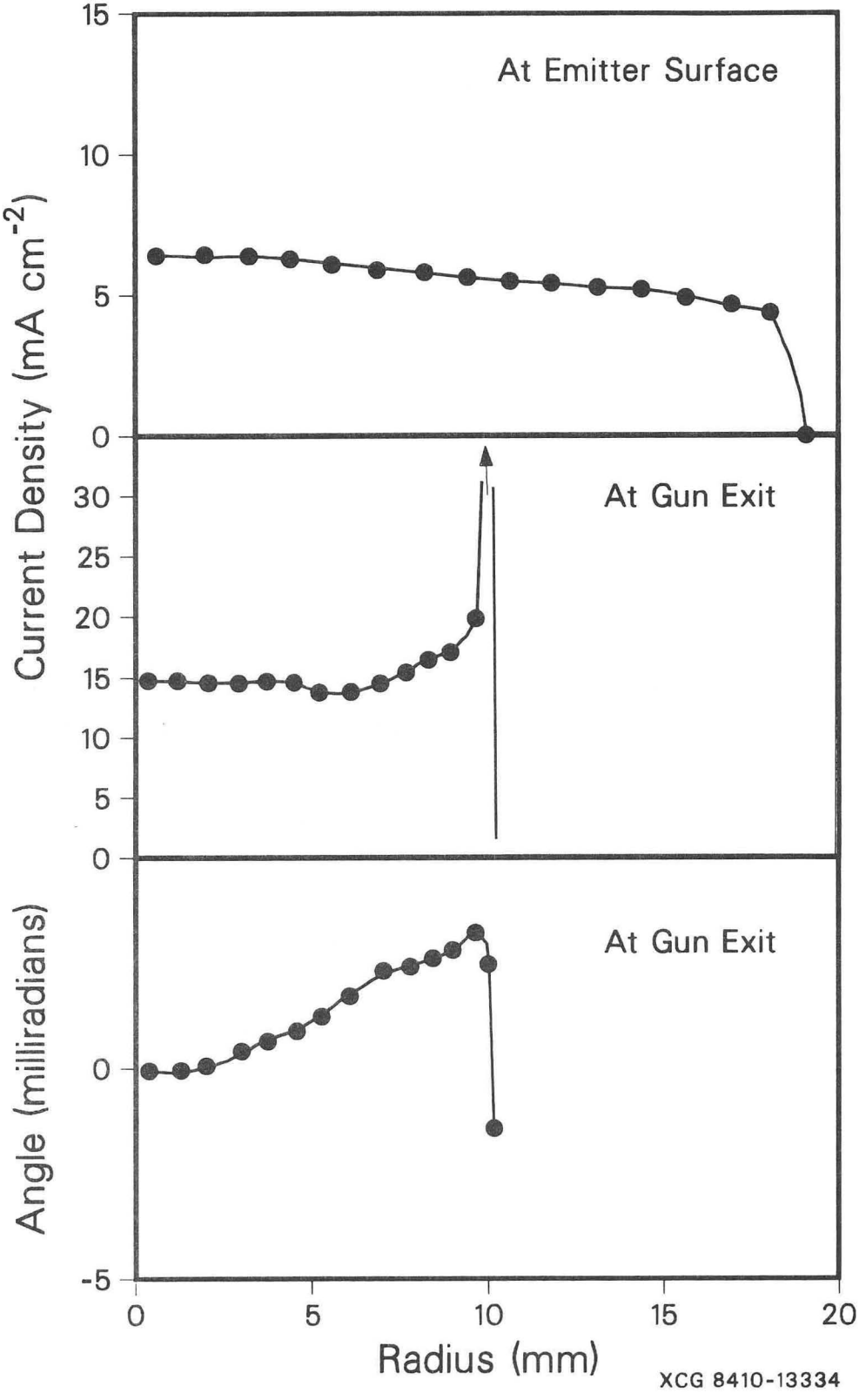

Figure 14. Beam profiles and divergence angles from the MBE-4 diode design.

2.4. Matching Section

The matching section will be made up of regular MBE4 quadrupole structures, with diagnostic boxes replacing the accelerating gaps. Figure 15 shows a K-V beam matched in such a structure. This is a larger current case, 10 mA at 200 kV. The gap before the first quadrupole is for steering, subsequent gaps are for diagnosis.

2.5. Fallback Position

This is a design that is feasible but may not produce emittance as low as is desired. For significant tune depression in MBE-4 one hopes for

$$\pi \epsilon_N = 1.5 \times 10^{-7} \pi \text{ m rad}$$

The proposed emitter structure lends itself to modification in the direction of four smooth tungsten or iridium hotplates, behind the same focussing electrode, at about the same temperature. These could be Cs coated by a collimated atomic beam from an oven in the centre of the ground plane. This approach would require some development and will be pursued only if the alumino-silicate emitters are not adequate.

Quadrupole	1	2	3	4	5	6	7	8
Aperture (mm)	28	28	28	28	22	22	22	22
ΔV (KV)	14	20.6	20.6	16	7.86	9.86	11.84	11.70

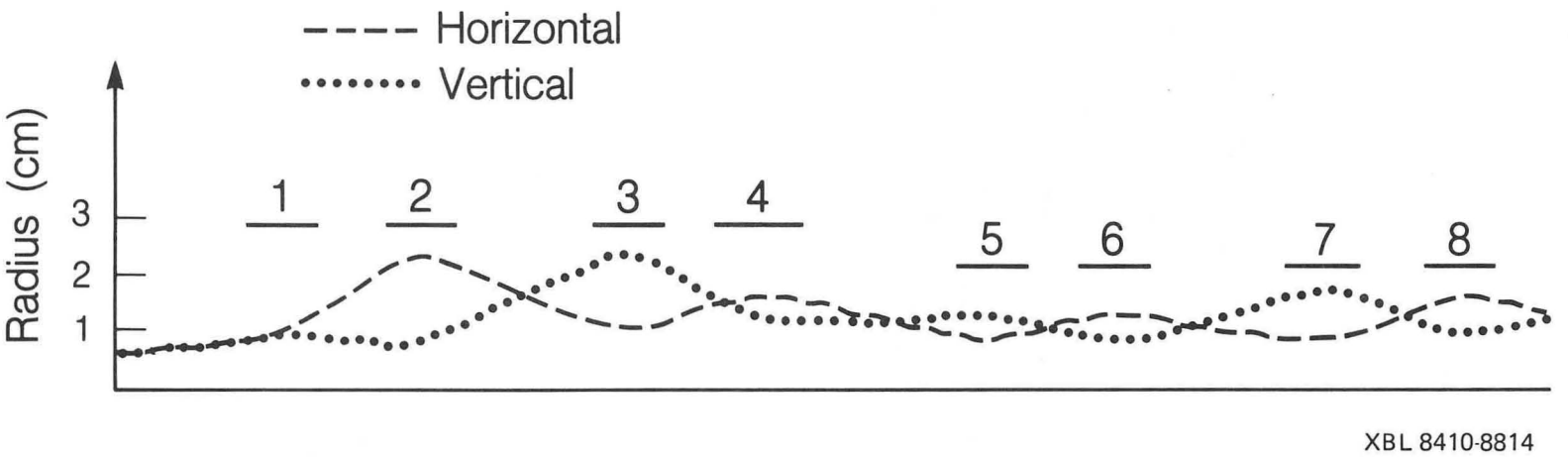

Figure 15. A matching solution for 10 mA of Cs^+ at 200 keV in MBE-4.

Induction Linac Component Development

(Faltens, Rosenblum)

1. 200 kV Test Stand

1.1. Astron Column Breakdown Voltage Measurements

As part of our continuing program to acquire engineering data relevant to large induction linac components, we have made voltage breakdown measurements on a brazed alumina column salvaged from the Astron injector*. This column consists of 22 sections of alumina, each alumina section 0.8 inches high, 9.5 inches inner diameter with a 3/8 inch wall thickness. The columns were brazed together with spun copper metal pieces. Since breakdown measurements are extremely sensitive to construction details, the results quoted here can be taken only as guidelines for future construction.

We mounted the column in the 200 kV Test Stand and evacuated the inside, the outside being surrounded with a mixture of air with 10% sulfur hexafluoride. We then measured the breakdown voltage of one, two and three sections of the insulator with dc applied voltage and with a pulsed voltage from our 200 kV Marx generator. The RC decay time of the Marx pulse was approximately 80 microseconds. The results are plotted in Fig. 16, and represent the highest values to which we felt the insulator could be conditioned without frequent breakdown. A criterion which we use is that the insulator should be operated at only one-half of the voltages shown if reliable performance is to be expected.

As can be seen from the figure, there does not appear to be a significant difference in performance between pulsed and dc conditions. In addition, we reversed the polarity of the dc voltage on a single section. The aim of this test was to investigate the practical impact of the sign of the electric field between metal and insulator. For dc, in any case, it is seen to have no perceptible effect on breakdown performance.

*N.C. Christofilos, R.E. Hester, W.A.S. Lamb, D.D. Reagan, W.A. Sherwood, and R.E. Wright. Rev. Sci, Instr. *35*, 886 (1964).

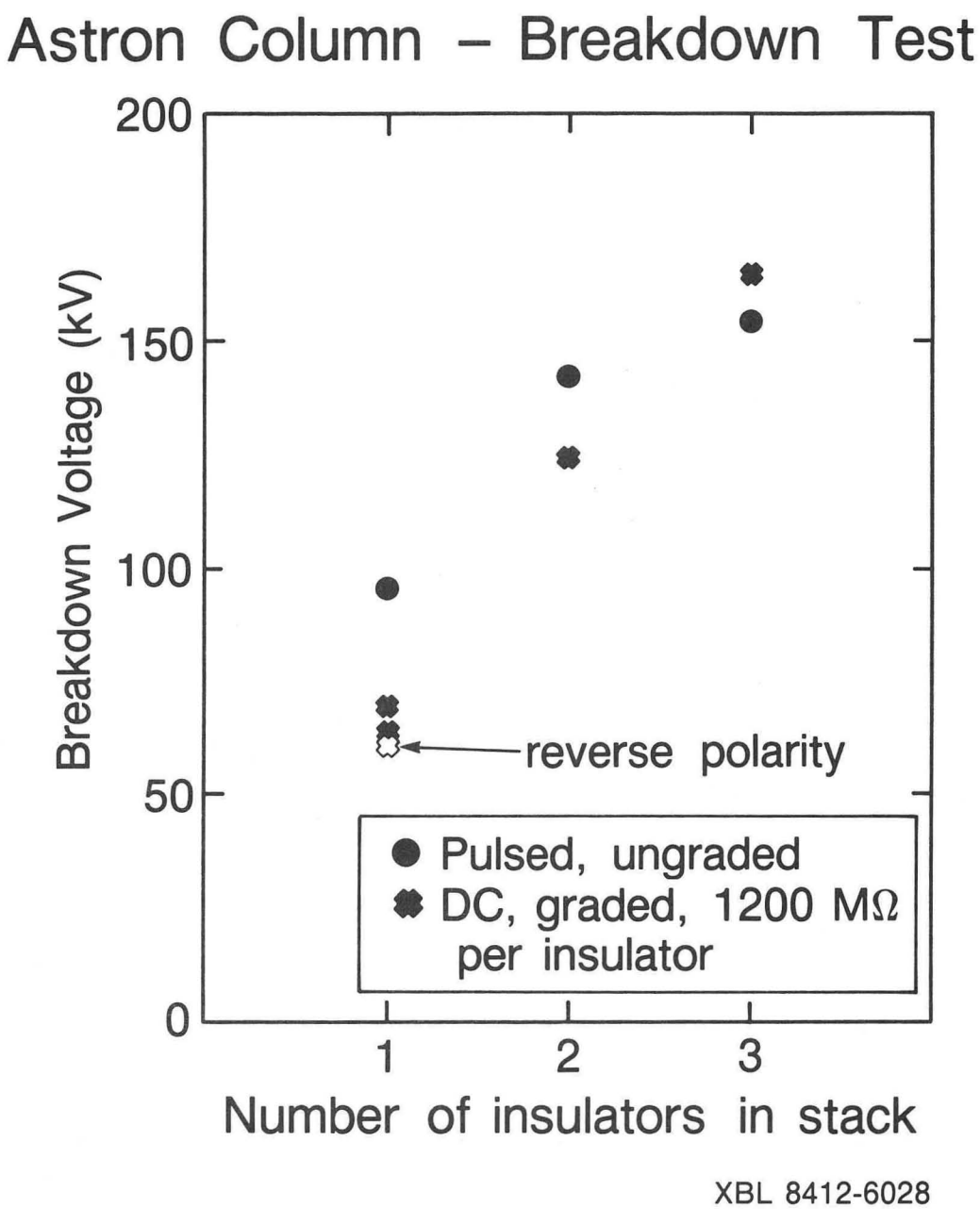

Figure 16. Breakdown tests of Astron column.

1.2. Conditioning Behavior of Insulators

Another important aspect of the practical use of insulators is their behavior as a function of conditioning. The test insulators were in the form of rods, 3/4 inches in diameter, and 12 inches long. The materials tested were installed as a leg of the insulator of the MBE-16 electrostatic quadrupole mockup described in our previous semi-annual report. The mockup was mounted in the vacuum space of the 200 kV Test Stand and, after pumping to a pressure of a few $\times 10^{-6}$ Torr, the voltage was raised until breakdown occurred along the test insulator. When the insulator began to hold this voltage, this was noted as a data point and the voltage was raised until the next breakdown occurred. The insulator was then left at this voltage until it conditioned up to this new value and so on. The tests were made using dc as well as pulsed voltage from the Marx generator.

The results for sintered alumina and fused quartz in Figs. 17 and 18, respectively show that the behavior of both insulators was quite similar. For dc as well as pulsed voltage the conditioning occurred over a time period of several hours. The changes in voltage holding were sometimes as large as a factor of two from beginning to end.

As a final test we examined the deconditioning behavior of the alumina insulator. For this test we began to measure the breakdown voltage of the insulator as a function of time after it had been conditioned up to its maximum dc voltage. The high voltage was turned on only long enough to probe the voltage at which the first breakdown occurred at a given time, and was then turned off and left off. The results are shown in Fig. 19.

The loss in voltage holding is quite dramatic, amounting to almost a factor of 3 over 100 hours in a vacuum of about 10^{-6} Torr. The conclusion to be drawn from this is primarily a cautionary one, to wit, that voltage holding in vacuum is only an approximate concept and this sort of degradative behavior must be taken into account in any vacuum insulator design for a practical device.

We are presently planning to improve the vacuum by an order of magnitude by using a cryopump on the Test Stand as well as to monitor the gasses desorbed by breakdowns.

2. Insulator Development

2.1. Outgassing Measurements

Work has continued throughout this reporting period on the automated vacuum outgassing apparatus. Programming of the Hewlett-Packard 85F to acquire, analyze, and plot the results has been completed. This reduces the labor of making measurements to merely one of loading samples into the vacuum system and starting the computer.

The system was used to continue the collaborative measurements with Ed Eaton at Los Alamos National Laboratory on various epoxy formulations for use as vacuum insulators. The following formulations were measured:

- LANL disc 2-DDS-U, a bisphenol A epoxy cured with aromatic diamine
- LANL disc 1-DDS-F, same as 2-DDS-F except filled to 70% by weight with 40 micron glass beads.
- LANL disc 3-1138/NMA-F, an anhydride cured epoxy novolac filled to 72% by weight with 40 micron glass beads.

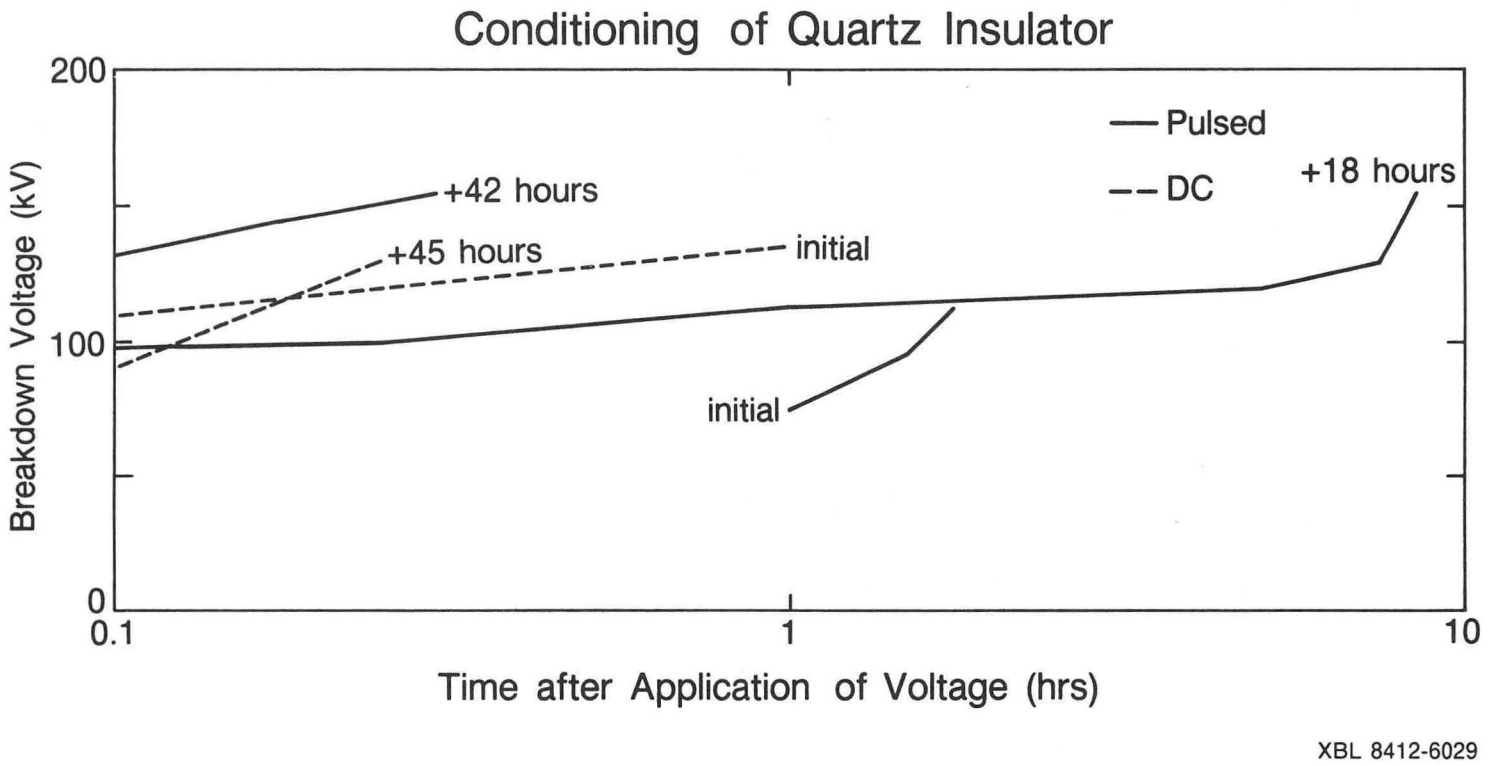

Figure 17. Conditioning of a quartz insulator.

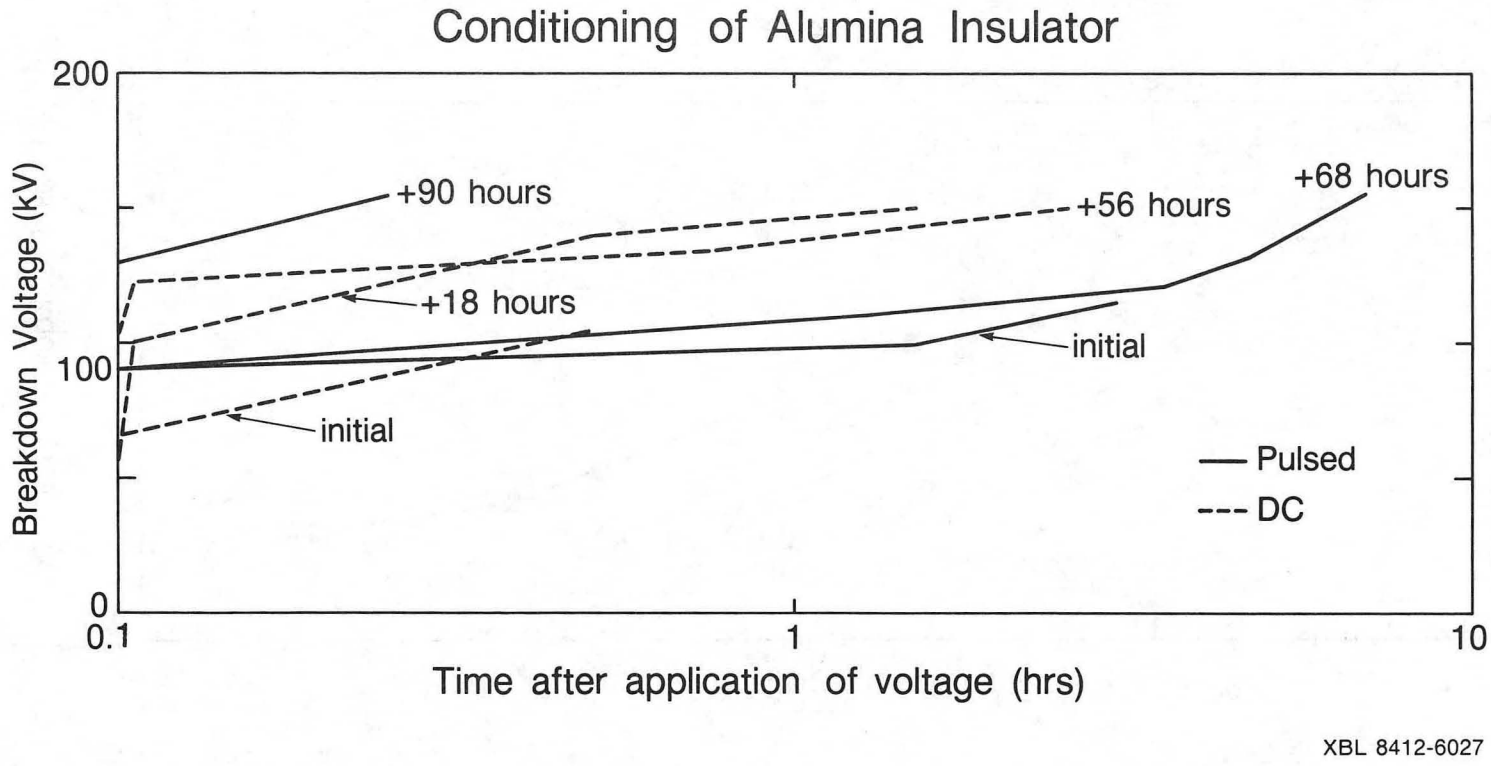

Figure 18. Conditioning of an alumina insulator.

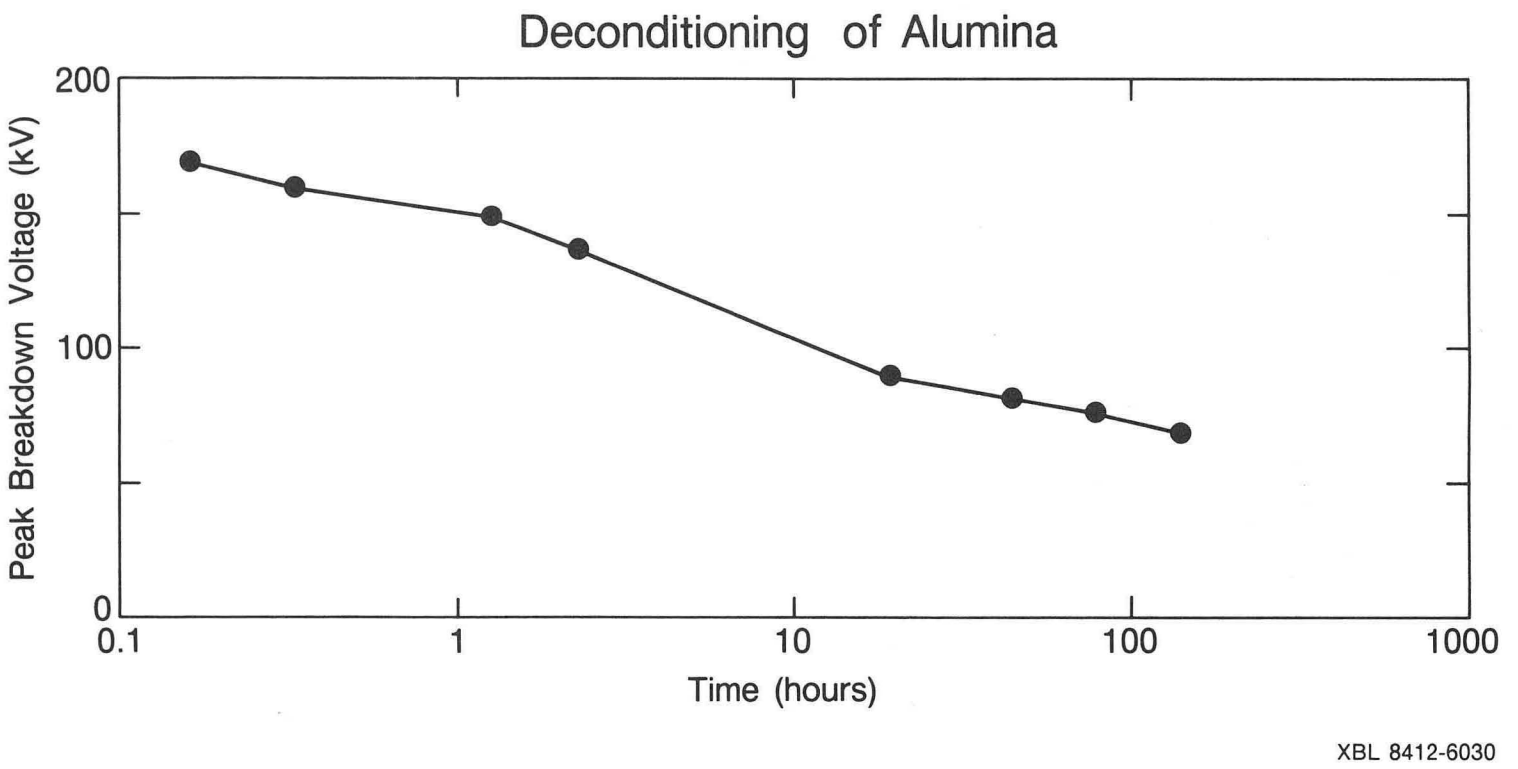

Figure 19. De-conditioning of an alumina insulator.

The results of the measurements are shown in Figs. 20, 21, and 22. The points labeled 1 are taken upon initial pumpdown, the points labeled 2 are taken during vacuum bakeout at 150°C, the points labeled 3 are taken following this bakeout. For the bisphenol A formulations, there is no significant difference between the filled and unfilled versions, except upon initial pumpdown where the filled formulation indicates a lower outgassing rate after long pumping times. The novolac formulation also seems quite similar to the bisphenol A, continuing a previously observed situation where most "good" plastics (Polysil, epoxies) have quite similar vacuum outgassing behavior.

2.2. Large Polysil® Insulator

The Polysil insulator fabricated using special stainless steel surface treatments mentioned in the previous semi-annual report was received on May 17, 1984. It was found to have two large vacuum leaks which were ground out with a diamond grinder and patched with Varian Torr-seal epoxy. During pressure checking, one of the bonds to the stainless steel end flange separated. Based on the applied pressure and the approximate contact area, the calculated peel strength of the Polysil-stainless steel joint was 50psi. This is too low to be used safely in an accelerator column. In spite of this, we decided to bond the test column back together using a 50:50 mixture of Epon Versamid 140 epoxy and Cab-o-Sil silica filler. This succeeded in producing a leak-tight assembly which we proceeded to test in our 200 kV Test Stand. With a vacuum of 2×10^{-6} Torr on the inside of the column and sulfur hexafluoride on the outside the insulator broke down across one of the 2-inch high sections at a voltage of 75 kV dc. After several discharges at this voltage, further vacuum leaks were opened in the insulator. Further tests were abandoned on this column. At this point we do not feel that we have made satisfactory progress towards a Polysil accelerator column because the molding techniques and bond strength to stainless steel are insufficiently well understood. Further work on Polysil has been discontinued in favor of work on Re-X and cast epoxy insulators, both of which are looking more promising at the moment.

2.3. Bonded Insulator Development

As a backup to brazed alumina and cast filled plastic insulators with metal embedments we have examined the feasibility of insulators made by bonding alternating sections of metal and insulator with various epoxies.

These studies were undertaken to test the tensile strengths of bonds between various insulator materials and stainless steel. The insulator materials selected for this study were pyroceram Re-X, 94% alumina and pyrex glass. Two adhesives were investigated — Bipax 2902, a silver-filled conducting epoxy, and Dexter-Hysol EA 9309, a chopped asbestos-fibre filled structural epoxy. Bonding surfaces were prepared, and bonds made as per HIFAN-261. Average tensile strengths were 3000 psi for Bipax 2902, and 6000 psi for EA 9309.

Three RE-X insulator rings (6 1/2 in. i.d., 7 3/4 in. o.d.) were bonded to stainless steel flanges using the conducting silver-filled epoxy adhesive Bipax 2902. A 10 cc. syringe was used to form a bead down the centre of the bond surface. A special applicator tool was developed to shape this bead to give a bond line thickness of approximately 0.005 in. under 10 psi pressure.

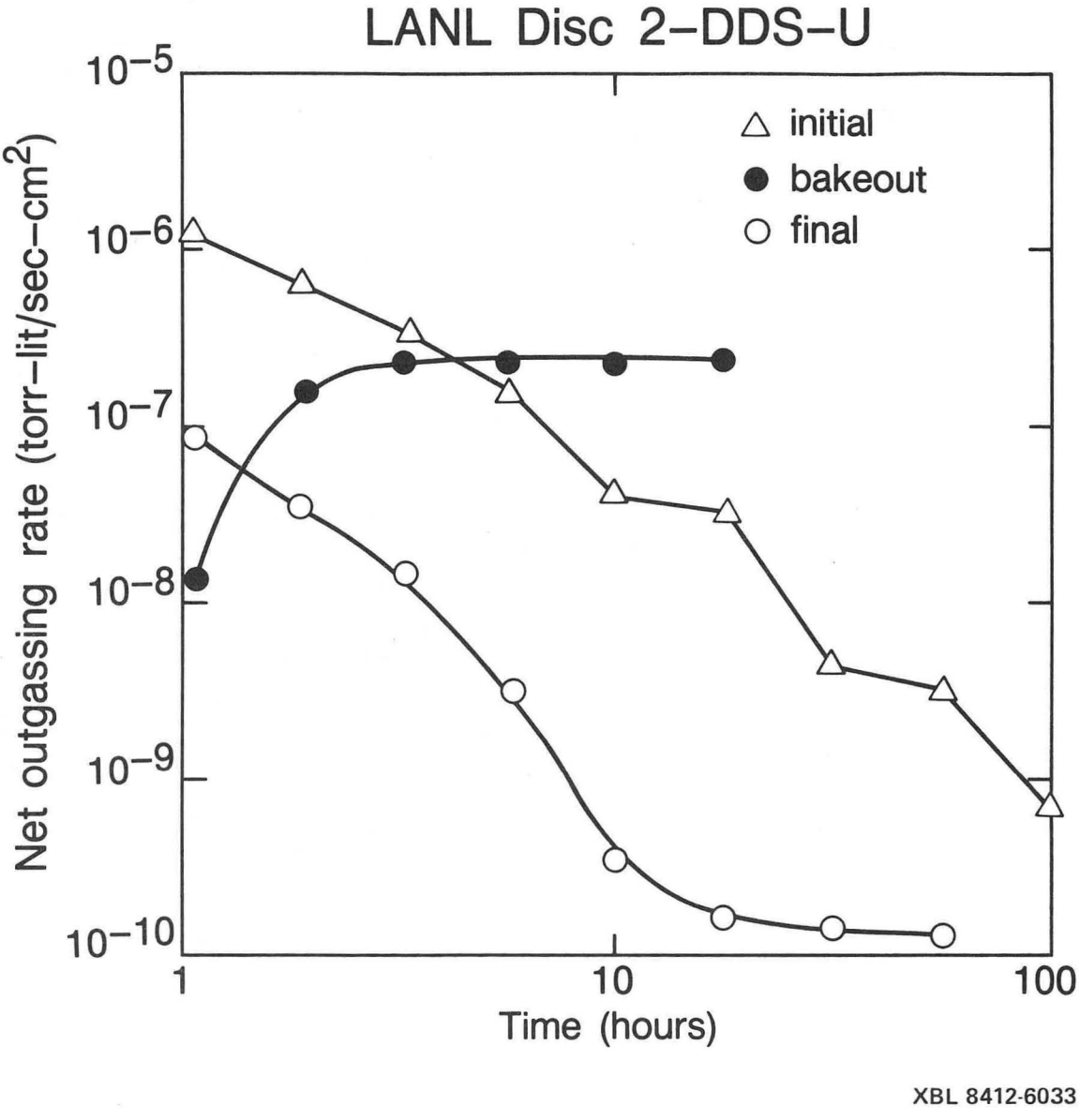

Figure 20. Vacuum outgassing of bisphenol A epoxy.

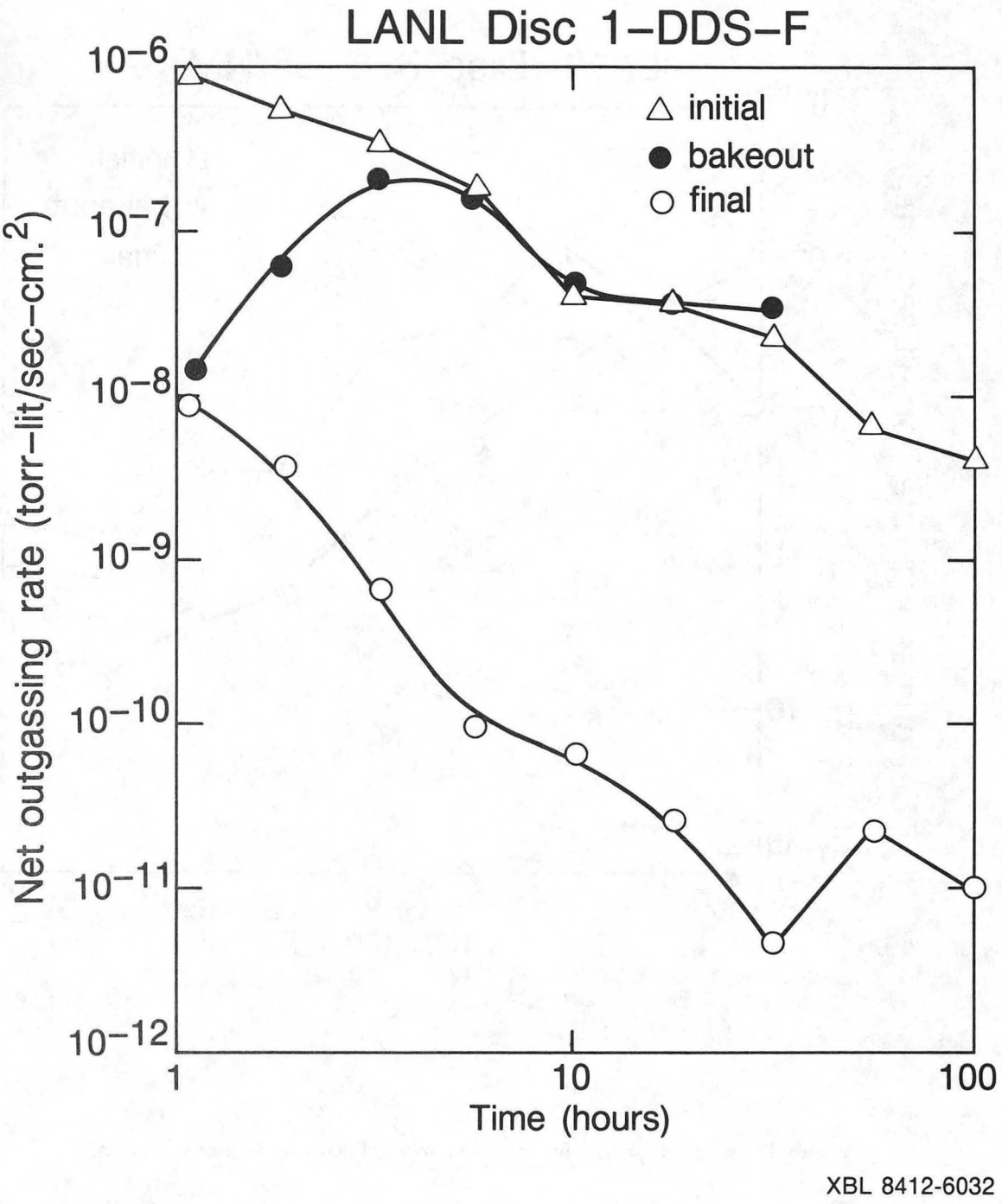

Figure 21. Vacuum outgassing of bisphenol A epoxy filled with 40 μm glass beads.

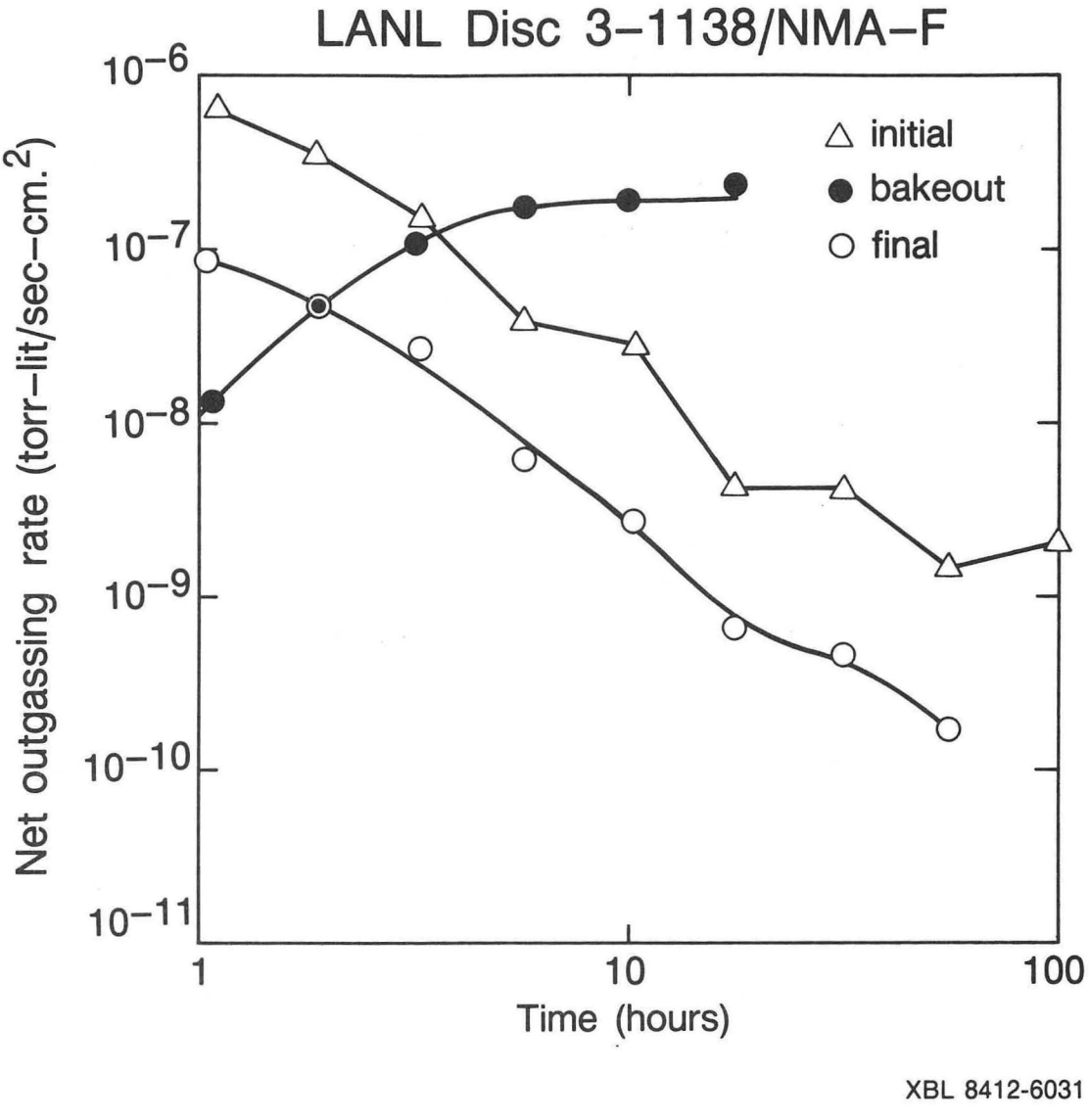

Figure 22. Vacuum outgassing of epoxy novolac filled with 40 μm glass beads.

This insulator was mounted in the 200 kV Test Stand with vacuum on the inside and 10% SF_6 in air on the outside. We applied dc voltage to a single insulator of the three ring stack. We were able to get the insulator to hold 50 kV after about 1/2 hour of conditioning. There were quite a few breakdowns which were initiated on the outside of the insulator (on the gas side). As a result, we decided to fill the outside region with freon liquid. This did not lead to any change in the results. Upon disassembly, the insulator was found to have grayish tracks in several places. The insulator was then completely taken apart for a post-mortem. The following possible flaws were noted:

- the insulator rings were not concentric with the metal rings.
- the epoxy had bled out beyond the edge of the insulator making a ragged edge.

If this technique is used in future assemblies we should try to use better jigs for assembly as well as to use glue line control techniques like those described by McDonnell-Douglas in the manufacture of the insulators for the MFE injectors.

2.4. Cast Epoxy Insulator Development

As another approach to the problem of manufacturing large diameter vacuum insulators for induction linac service we have begun a program to examine several formulations of filled epoxies. These formulations have been selected based on measured and expected mechanical and electrical performance.

Five filled-epoxy insulator formulations are being studied comparing first the epoxy resins: systems based on Diglycidylether of Bisphenol-A (e.g. Epon 826) are tougher (less brittle) than those based on cycloaliphatic epoxies (e.g. ERL 4221). Hence the cycloaliphatic epoxy-based systems require the incorporation of modifiers to provide flexibility and higher impact strengths. Excessive amounts of modifier will reduce the Deflection Temperature under Load (DTUL), and increase the tendency of the material to creep. However, cycloaliphatic epoxy-based systems have better arc and arc-track resistance, because the material will oxidize, leaving no carbon residue.

Comparing curing agents, anhydrides (e.g. Hexahydrophthalic anhydride-HHPA) give higher DTUL, and have better electrical properties than amines (e.g. D-230). However, the ester link formed during anhydride cure is more subject to hydrolysis than the C-N bond in amine cured systems. Also, the C-N bond is more chemically resistant than the ester bond. D-230/Epon 826 is a room temperature curing system, and that has definite advantages over the high temperatures required for anhydride cures.

Comparing fillers, aluminum trihydrate (ATH) provides better arc track resistance than silica. However, it is a poor reinforcing filler, and the filled system is poorer in mechanical strength than the unfilled system. It is easy to machine using ordinary tools, whereas silica-filled insulators require strictly diamond tools. The reinforcing capabilities, and thus the impact and tensile strengths of insulators filled with ATH and/or silica can be improved by treating the fillers with a silane coupling agent.

These formulations will be tested electrically, and mechanically in the next few months.

3. Metglas Core Tests

Our continuing collaboration with Allied Corporation to engineer an induction linac core package using their Metglas^R amorphous magnetic glass ribbons has proceeded vigorously in this reporting period.

The materials we have investigated thus far using small cores are Metglas^R 2605SC, 2605CO, and 2605S-2. In the near future, we are planning to examine Metglas^R 2605S-3A. We have investigated the DC hysteresis loops and pulsed magnetic behavior including losses/pulse for pulse widths from tens of microseconds down to $< 1\ \mu s$ as would be required in an induction linac for heavy ions. In addition to cores manufactured by the standard method of annealing the finished cores in an applied field (here called "box annealed") we have also examined cores made from as-cast material as well as material which was rewound into finished cores after annealing. The rewound material was first magnetically annealed on supply spools of 2 inch inner diameter, then rewound inside out, then backwound inside out again and interleaved with 1/4 mil mylar. This procedure is expected to minimize residual stresses in the final core. The hope of this latter exercise was to reduce the eventual size of ovens required to anneal full-sized cores.

The results of these tests indicate that the as-cast material is not attractive for this application whereas the rewound material appears to be a viable option.

3.1. Experimental Results

The DC hysteresis loops of all of the test toroids were initially measured to 80 A/m (1 Oe) by Carl Smith of Allied Corp. using a Magnos MTS Hysteresisgraph. The toroids were typically 0.6 kg in weight with 2 inch inner diameter, 3 inch outer diameter, and 2 inch height. Pulsed loss measurements were made using a thyratron pulser consisting of a English Electric Valve CX 1159 thyratron discharging a 1.37 microfarad capacitor through the test core. The voltage/turn across the core in one winding and the ampere-turns flowing through a second winding were measured using a Tektronix Model P6015 high voltage probe and a Pearson Model 411 current transformer respectively. They were photographed using a Tektronix Model 7844 dual beam oscilloscope. Prior to the measurement, the core was reset to "negative" remanence by using a small dc current or by using a diode string across the thyratron such that it carried the reversal current resulting from the discharge of the energy stored in the core (ringback reset). Thus, the flux swing typically measured is the sum of B_r and B_s, for square loop materials. A typical set of dc magnetic data is shown in Fig. 23 and typical pulsed data are shown in Fig. 24. The maximum applied H in both cases is approximately the same and of the order of a few Oe.

The pulsed loss measurements/cycle are summarized in Fig. 25. The flux swing corresponding to the loss data is indicated in Table II. It is clear in all cases that the as-cast material has about half the useful flux swing of the box-annealed material. The behavior of the rewound material is quite similar to the box annealed material in all cases, indicating that, at least for the small cores, the handling associated with unwinding and rewinding the materials after field annealing does not do any severe damage to its performance in induction linac service. A more quantitative comparison of the various materials and treatments will be given in the next section.

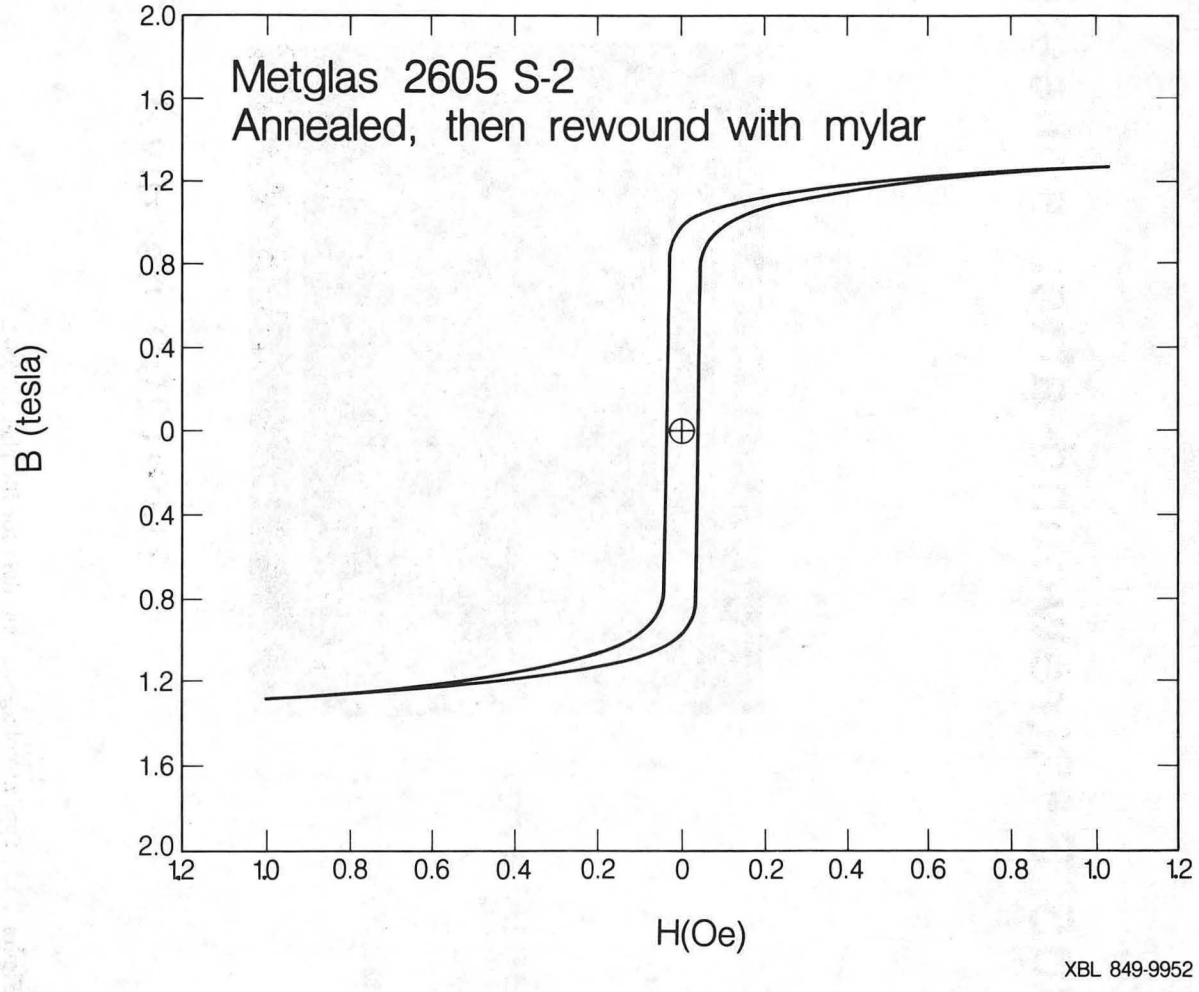

Figure 23. DC hysteresis loop for Metglas 2605S-2 (f = 0.1 Hz).

Metglas 2605 S-2(rewound after annealing)

Core voltage(50 V/turn-div.)

"Useable" current level

Drive current(20 A-turn/div.)

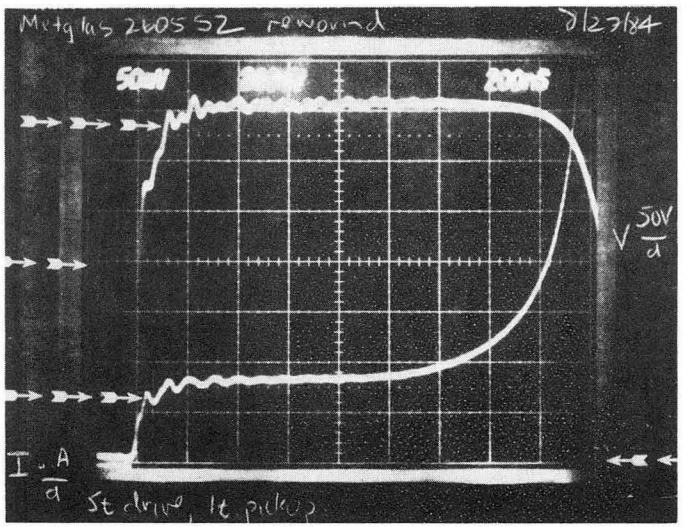

Zero level

Time(200 ns/div.)

Figure 24. Typical voltage-current data for Metglas 2605S-2.

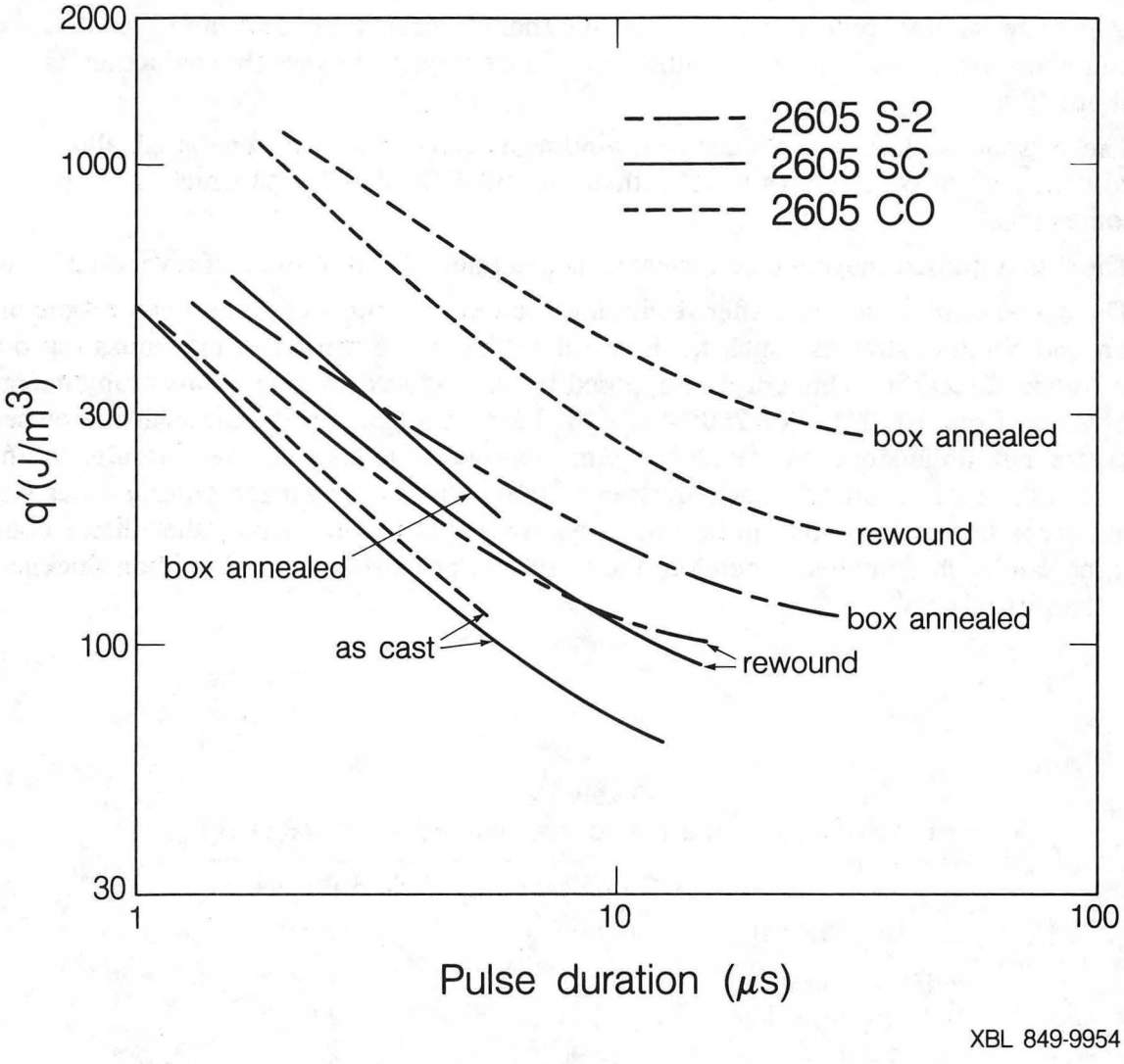

Figure 25. Pulsed loss data adjusted for stacking factor, f = 1.

A comparison of the magnetic performance resulting from the dc and pulsed measurements is given in Table II. For most examples, pairs of toroids were measured — one at LBL and one at Allied. The following results are apparent from the data in the table:

The flux swing in pulsed service is smaller than the dc value, taken here as $B_r + B_{80}$. The largest reductions are for the box annealed 2605SC and 2605S-2 materials(about 20%). For all other conditions reported here the reduction is about 10%.

The loss in dc flux swing due to rewinding is larger for the iron based alloys 2605SC and 2605S-2 (typically 20%) than for 2505CO (about 10%) which contains some cobalt.

The loss in pulsed magnetic performance is less than 10% as a result of rewinding .

The decrease in remanence after rewinding is due to the interaction between magnetostriction and bending stresses which tends to rotate the easy direction of magnetization out of the ribbon direction. This effect is opposed by the induced magnetic anisotropy energy which ranges from 100 J/m^3 for 2605SC to 1000 J/m^3 for 2605CO.[3] Although the pulsed results are not understood in detail it seems reasonable to ascribe these results to the dynamics of domain motion. Magnetization of these alloys at the magnetization rates studied proceeds primarily by the motion of ribbon-spanning bar domains rather than ribbon encircling sandwich domains. Therefore the losses are proportional to the ribbon thickness rather than its square.[4]

Table II.
Comparison of dc and pulsed magnetic behavior. ($B_r + B_r$)

Metglas Material	DC flux swing (Tesla)	Pulsed flux swing (Tesla)
2605SC as cast	1.2	1.1
box annealed	2.7	2.0
rewound	2.4	2.0
2605S-2 as cast	—	—
box annealed	2.9	2.2
rewound	2.2	2.0
2605CO as cast	1.2	1.1
box annealed	3.4	3.1
rewound	3.0	2.7

3. C. H. Smith and D. M. Nathasingh, *IEEE Conf. Record 16th Power Modulator Symp.*, Arlington, VA, June 1984, p. 240.
4. C. H. Smith, D. Nathasingh, and H.H. Liebermann, to be published in *IEEE Trans. Mag.* (1984 Intermag Issue).

3.2. Conclusions

The design of a minimum cost induction accelerator for use as a fusion driver involves making choices among a large variety of components including: core material, capacitors, switch tubes, focussing elements, vacuum system. Because the choices interact with with one another in the total machine cost, computer analysis has been used to investigate various options.[5] One way at looking at purely the core material performance is by picking some "reference" induction unit design and looking at the total losses in this "reference" unit as a function of pulse width. This is done in Fig. 26 for the three materials reported in this paper as well as for 2 mil thick silicon steel and 1 mil nickel-iron. In terms of purely the core losses in the module, the 2605SC and 2605S-2 appear to have the lowest losses. Since they are less expensive than the 2605CO they would appear to be the most cost effective alloys to choose at this time.

5. Andris Faltens, Egon Hoyer, Denis Keefe, and L. Jackson Laslett, IEEE Trans. Nuc. Sci. *NS-26*, 3106(1979)

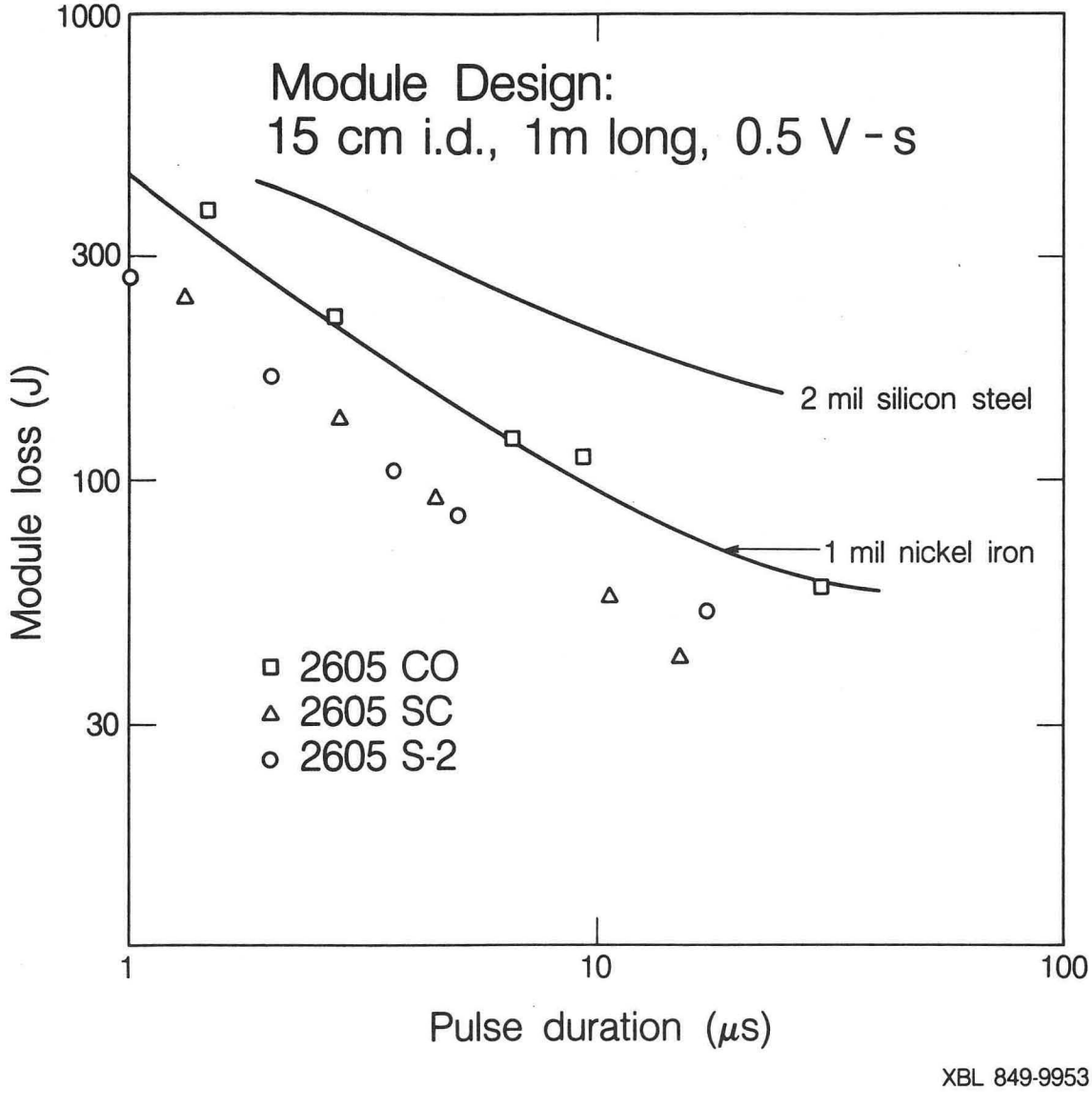

Figure 26. Induction module design exercise showing improved performance for Metglas 2605SC and 2605S-2.

Publications

HI-FAN-249 LBL-17657	H.I.F. Staff	Heavy Ion Fusion Half-Year Report October 1, 1983 – March 31, 1984
HI-FAN-250 LBL-17788	T.J. Fessenden R.T. Avery V. Brady J. Bisognano C. Celata W.W. Chupp A. Faltens E.C. Hartwig D.L. Judd D. Keefe C.H. Kim L.J. Laslett E.P. Lee S.S. Rosenblum L. Smith A. Warwick	Induction Linacs for Heavy Ion Fusion Research (Proceedings of the 1984 Linear Accelerator Conference, May 7–11, 1984, Seeheim/ Darmstadt, Fed. Rep. of Germany)
HI-FAN-251	L. Smith	Effect of Random Quadrupole Misalignments in MBE (6/84)
HI-FAN-252 LBL-17528	A. Faltens D. Keefe C. Kim S. Rosenblum M. Tiefenback A. Warwick	Quadrupole Transport Experiment with Space Charge Dominated Cesium Ion Beam (Proceedings of the 1984 Linear Accelerator Conference, May 7–11, 1984, Seeheim/ Darmstadt, Fed. Rep. of Germany)
HI-FAN-253 LBL-17754	D. Keefe R.O. Bangerter T.F. Godlove W.B. Herrmannsfeldt	Heavy Ion Fusion Accelerator Research in the U.S. (Presented at Xth IAEA Conference on Plasma Physics and Controlled Fusion Meeting, London, Sept. 12–19, 1984)
HI-FAN-254	M.C. Lampel	(Ph.D. Thesis) An Intense Non-Relativistic Cesium Ion Beam (February 1984).
HI-FAN-255	T. Fessenden C. Kim	Foreign Trip Report: May 5–19, 1984. Linac Conference in Darmstadt/Seeheim, FRG.

HI-FAN-256	Magnetic Fusion Group	Abstracts Submitted for the Twenty-Six Annual Meeting, Division of Plasma Physics. To be presented at the Twenty-Six Annual Meeting of the Division of Plasma Physics of the American Physical Society, Boston, MA, October 29 – November 2, 1984 (9/24/84)
HI-FAN-257	HIF Group	Heavy Ion Fusion System Assessment Project. Scope of Work to be Perfomed at LBL. Funded by DOE Office of Energy Research-of Program Analysis (9/84)
HI-FAN-258	Victor Brady	Harmonic Analysis of the Electrostatic Potential Due to an Array of Round Rod Quadrupoles for Focusing a Group of Four Beams. (9/84)
HI-FAN-259 PUB-5127	HIFAR Group	Revised HIFAR Program Plan for FY 85 (9/19/84)
HI-FAN-260 LBL-18426	A. Faltens S. Rosenblum C. H. Smith	Investigation of Metglas Toroid Fabrication Techniques for a Heavy Ion Fusion Driver
HI-FAN-261	Naseem Munshi	Adhesives for Bonding Stainless Steel to Ceramic and Glass Insulations (an engineering note)
HI-FAN-262	A. Faltens D. Keefe C.H. Kim	Foreign Travel Report: INS International Symposium on Heavy Ion Accelerators and their Applications to Inertial Fusion January 23–27, 1984 Institute for Nuclear Studies University of Tokyo, Japan
HI-FAN-263	D. Keefe	Foreign Travel Report: Workshop on the Generation of High Energies, Laboratori Nazionali dell'INFN, Frascati, Italy September 25 – October 1, 1984 (10/84)

H.I.F. Staff Roster

Denis Keefe

Robert T. Avery
Clarence Chavis
Warren Chupp
Edwin R. Edwards
Andris Faltens
Thomas J. Fessenden
David Gough
Edward C. Hartwig
T. Henderson
Charles H. Kim
John Meneghetti
N. Munshi
Chester D. Pike
Stephen S. Rosenblum
Gerald L. Stoker
Michael Tiefenback
David Vanecek
Anthony Warwick

Lloyd Smith

Joseph Bisognano
Victor Brady
Christine Celata
D. L. Judd
Geoffrey Krafft
L. Jackson Laslett
Edward P. Lee

William B. Herrmannsfeldt, SLAC

End of the Year Report: Distribution List

Allied Chemical Corporation

Carl Smith

Argonne National Lab.

Thomas A. Fields
Ronald Martin

University of Arizona

R. Morse

Batelle

John Hartman

Bechtel

W. Allen

Brookhaven National Lab.

Mark Barton
E. Courant

C.E.A. Bruyeres-le-Chatel

R. Dei-Cas

University of Calif., Irvine

Norman Rostoker

University of Calif., Riverside

Robert Poe

Cornell University

John Nation
Ravi N. Sudan

DARPA

Joseph Mangano

Department of Defense (SDIO)

Richard Gullickson
Gerold Yonas

Department of Energy

DP-OIF

Sheldon L. Kahalas
L. Killion
R. Schriever
Marshall Sluyter
Col. Charles Whited

ER

Terry Godlove
James S. Kane
Richard Kropschot
James Leiss
Gerry Peters
David F. Sutter
Alvin Trivelpiece, Dir.,
Office of Energy Research
William Wallenmeyer

DOE San Office

Rudolf Bredderman
Dennis Neely

E.P.R.I.

Robert Scott

Fermi National Accelerator Lab.

Frank T. Cole
Fred Mills
Lee Teng

GANIL

P. Lapostolle

GSI

R. Bock
D. Boehne
I. Hofmann

University of Illinois

G. Miley

Institute for Nuclear Study

Y. Hirao

KMS Fusion, Inc.

Alex Glass
Michael J. Monsler

Kanazawa University

S. Kawasaki

Lawrence Berkeley Laboratory

R. Avery, 46/189
K. Berkner, 50/149
J. Bisognano, 47/112
W.W. Chupp, 47/112
T. Elioff, B46B
A. Faltens, 47/112
T. Fessenden, 47/112
A. Garren, 47/112
D. Gough, 47/112
H. Grunder, 50A/4119
E. Hartwig, 47/112
H. Heckman, 50/245
T. Henderson, 46/161
E. Hoyer, 46/187
E. Hyde, 50A/4133E
R. Johnson, 50A/4119
D. Judd, 47/112
D. Keefe, 47/112
C. Kim, 47/112
M. Krebs, 50A/4112
W. Kunkel, 4/230
G. Lambertson, 47/112
L.J. Laslett, 47/112
E.P. Lee, 47/112
E. Lofgren, 47/112
J. Marx, 50/149
J. Meneghetti, 46/161
J. Peterson, 47/112
S. Rosenblum, 47/112
A. Sessler, 4/230
D. Shirley, 50A/4113
L. Smith, 47/112
D. Vaughan, 50/149
A.I. Warwick 47/112

Lawrence Livermore Laboratory

Roger Bangerter, L-477
Richard J. Briggs, L-321
John L. Emmett, L-488
John Holzrichter, L-481
William Krupke, L-488
Jim Mark, L-477
John Nuckolls, L-477
Louis Reginato, L-526
Erik Storm, L-481

Lockheed

John Siambis

Los Alamos National Laboratory

Ihor Bohachevsky
Richard Cooper
Robert Jameson
Don Kerr
Edward Knapp
Earl Meyer
Roger B. Perkins
Steve Rockwood
Henry Rutkowsky
Richard Stokes
Tai-Sen Wang

University of Maryland

Martin Reiser
Derek Tidman

Max Planck Inst. fur Plasma Physik Garching

Arnulf Schluter

Maxwell Laboratories

Library

National Bureau of Standards

S. Penner
M. Wilson

Naval Research Lab.

Steven Bodner
T. Coffey
Irving Haber
Philip Sprangle
Peter Turchi

Occidental Research Corp.

Wyn Salisbury

Osaka University

T. Mochizuki
C. Yamanaka

Universita di Padova

A. Pascolini
M. Pusterla

Physical Dynamics

G. H. Gillespie

Physics International

Library

Pulse Sciences, Inc.

Ian Smith
Ken Riepe

RAFAEL

Joseph Shiloh

Rutherford Laboratory

John D. Lawson
Chris Pryor

Sandia Laboratories

Everet H. Beckner
Don Cook
Glenn Kuswa
Tom Martin
J.P. Vandevender

Soka University

Tetsuya Saito

SOREQ Nuclear Research Center

A. Sternlieb

SLAC

William Herrmannsfeldt, Bin 26
Burton Richter, Bin 7

TRW

J. Gordon
Z. Guiragossian
J. Maniscalco
A.W. Maschke
W. Steele

Westinghouse

M. Nahemow
E. W. Sucov

University of Wisconsin

G. Kulcinski
G. Moses
R. Peterson

TECHNICAL INFORMATION DEPARTMENT
LAWRENCE BERKELEY LABORATORY
UNIVERSITY OF CALIFORNIA
BERKELEY, CALIFORNIA 94720